POLITECNICO DI TORINO

Master's Degree in Nanotechnologies For ICTs

Master's Degree Thesis

Investigation of Elastic Topological Protected Interface Modes on RF Piezo-Electric MEMS Technology

Supervisors

Prof. Fabrizio GIORGIS

Prof. Cristian CASSELLA

Candidate

Tommaso MAGGIOLI

December 2023

Abstract

Since their discovery, *topological insulators* have attracted significant research interest due to their nontrivial topological properties. These properties give rise to the emergence of edge states that propagate along the interface between inversed topological invariants. These edge states assume great relevance because of their ability to resist perturbations and so being immune to back-scattering. For these reasons, they are referred to as topologically protected states. The discovery of this phenomenon in quantum systems and the potential of this unidirectional transport with negligible attenuation inspired and led to the demonstration of the equivalent *topological edge states* in acoustic technologies.

The aim of this work is to investigate the existence of topologically protected states at the interface of a Piezo-Electric MEMS device working in the RF range. A topological edge mode is formed when a break of the symmetry of a periodic system with a topologically non-trivial bandgap happens. To achieve this outcome, we examined a piezoelectric metamaterial based on AlScN, which has a spatially periodic structure that ensures a symmetric band-structure.

A detailed examination of the band structure of the device's single unit-cell was conducted. The presence of topologically-protected modes was initially investigated through numerical methods, specifically the finite element method (FEM). The Floquet boundary condition was applied to the single unit-cell during this study. The existence of this state was then verified by calculating the Zak phase, which is a geometric phase characterizing the topological properties of bulk bands in a 1D periodic system. To investigate the presence of topological-protected modes in a device with a finite number of unit cells, a numerical study was again carried out using FEM simulations

Acknowledgements

I want to thank my supervisor prof. Cristian Cassella for his support and for giving me the opportunity to do research at Northeastern University.

I also want to thank Ph.D. Xuanyi Zhao, who followed and helped me step by step in this new journey.

Thanks to all my friends who, no matter how elusive I can be, never stop being there. A special thanks to Nicolò and Paolo, who welcomed me into their home and taught me how to survive the polytechnic.

Thank you to those who showed me that I can be an Ulysses of this world.

Many thanks to my parents and my sister, who, no matter how hard I try to increase the kilometers from them, have never stopped supporting me, and I always carry them with me.

A never big enough thank you to Chiara. I wouldn't be here without your support, your complicity, and without knowing how much you believed in me.

And thanks to me, because in the end, *ce la posso fare*

"Dai un calcio alla ragione e fai spazio all'impossibile"

Table of Contents

List of Tables

List of Figures

Acronyms

2DRR 2D Resonant Rods

AVHE Acoustic Valley Hall Effect

BZ Irreducible Brillouin zone

CMR Counter Mode Resonator

DC Dirac Cone

DP Dirac Point

FBAR Film Bulk Acoustic Resonator

k Wave Number

PC Phononic Crystal

ω Circular Frequency

QHE Quantum Hall Effect

QSHE Quantum Spin Hall Effect

QVHE Quantum Valley Hall Effect

SIS Space Inversion Symmetry

TRS Time Reversal Symmetry

Chapter 1

Introduction - Topological state in acoustic system

1.1 Acoustic Wave propagation

The study of how elastic waves propagate through materials with a periodic structure has been a topic of interest in science since a long time ago. However, in the early 1990s, works such as those by Sigalas et al. [1] and Kushwaha et al. [2] on phononic crystals (PC) have reignited interest in this area of research. In several materials being studied, certain important physical properties (like their elastic moduli and density) exhibit periodic variation based on their position in the material. This leads to interesting properties such as frequency band gaps and negative refraction. The investigation of the propagation of elastic waves in these periodic structures requires theoretical elements derived from the study of solid-state physics, such as the direct and reciprocal lattice, the unit cell, dispersion relations, and the irreducible Brillouin zone. Furthermore solving the equations of elastic wave propagation will be required.

1.1.1 One dimensional Atomic Chain

Single Atom Per Unit Cell

Let's start by examining the most basic periodic structure, which is an infinite linear chain of atoms in one dimension. All atoms have the same mass, denoted by m, and are aligned along the x axis. The adjacent atoms are connected by a spring with a stiffness of β and, at equilibrium, the distance between them is a. Therefore, the equilibrium position of the n atom is $x_{n,eq} = na$. Atoms can move slightly around their equilibrium position. Thus, at time t, the position of an atom can be expressed as $x_n(t) = na + u_n(t)$, where $u_n = x_n - x_{n,eq}$ represents the displacement of the n_{th} atom from its equilibrium position and $|u_n(t)| << |x_n(t)|$.

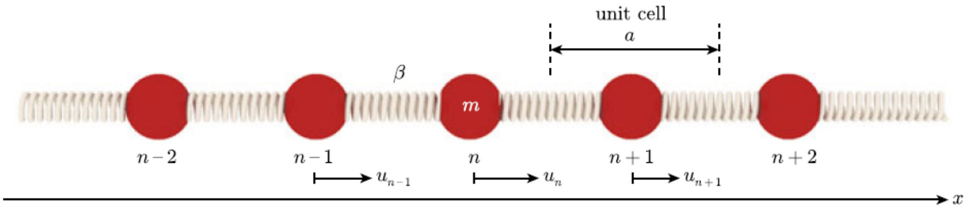

Figure 1.1: Illustration of the 1D atom chain with a single atom as unit cell

As seen in Fig. 1.1, the structure being considered consists of a single atom, the unit cell, that is repeated along the x direction with a periodicity of a. Due to this, we can apply Newton's second law to the n_{th} atom to understand its interaction with its closest neighbors:

$$m\frac{\partial^2 u_n}{\partial t^2} = -\beta(u_n - u_{n-1}) + \beta(u_{n+1} - u_n) = \beta(u_{n+1} + u_{n-1} - 2u_n) \tag{1.1}$$

Searching for solutions in the form of sinusoidal propagating waves of amplitude U_0 such as $u_n(t) = U_0 e^{i(kna-\omega t)}$ where k is the wave number and ω the circular frequency, Eq(1.1) becomes:

$$-m\omega^2 = \beta(e^{ika} + e^{-ika} - 2) = 2\beta(cos(ka) - 1) = -4\beta sin^2\left(\frac{ka}{2}\right) \tag{1.2}$$

From this equation is possible to obtain the relation between the circular frequency ω and the wave number k, which is defined as the *dispersion relation*:

$$\omega(k) = \sqrt{\frac{4\beta}{m}}\left|sin\left(\frac{ka}{2}\right)\right| \tag{1.3}$$

but being $|sin(ka/2|$ a $\pi - periodic$ function

$$\left|sin\left(\frac{ka}{2}\right)\right| = \left|sin\left(\frac{ka}{2} + \pi\right)\right| = \left|sin\left(\frac{a}{2}\left[k + \frac{2\pi}{a}\right]\right)\right| \tag{1.4}$$

also $\omega(k)$ is a periodic function of k with periodicity $G = 2\pi/a$ and $\omega(k+nG) = \omega(k)$ where n is an integer number. Therefore, it is possible to say that the propagation mode with a wave number of $(k+G)$ is equivalent to the one with a wave number of k. The lattice parameter a is linked to the direct lattice, while the periodicity $G = 2\pi/a$ is linked to the reciprocal lattice.

Because of the periodic nature of the dispersion relation in reciprocal space, essential information about the vibration modes that can travel in the chain can be found in within the wave numbers in the range between $-\pi/a$ and π/a. This specific range, centered in $k = 0$ is commonly referred to as the *first Brillouin zone* of the reciprocal lattice. As a result, the dispersion relation also exhibits symmetry with respect to the $k = 0$ plane, enabling us to focus our study on the *irreducible Brillouin zone* (BZ), which is the domain where the wave numbers ranging from 0 to π/a.

Two Atoms Per Unit Cell

Let's take a closer look at a complex structure, which is an infinite one-dimensional linear chain made up of unit cells, each of them containing two atoms with different masses, as shown in Fig.(1.2). In this new setup, the lattice parameter is $2a$, and all the springs are assumed to possess the same stiffness represented by β. It is possible to categorize the atoms as *even atoms*, the ones with mass equal to m_1, and *odd atoms* with mass m_2 and labeling them with $2n$ and $2n + 1$ respectively, where n is an integer number.

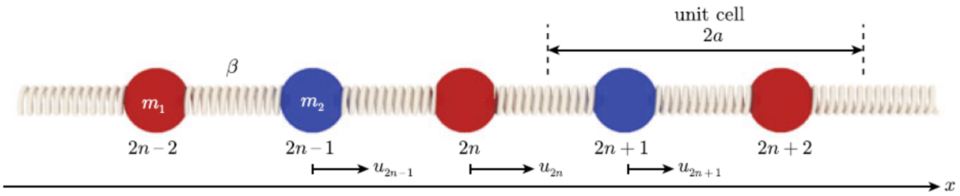

Figure 1.2: Illustration of the 1D atom chain with two atoms of different masses as unit cell

Following the same assumption made for the case of the single-atom unit cell, we can formulate the equation of motion for both the *even* and *odd* atoms:

$$\begin{cases} m_1 \dfrac{\partial^2 u_{2n}}{\partial t^2} = -\beta(u_{2n} - u_{2n-1}) + \beta(u_{2n+1} - u_{2n}) \\ \qquad\qquad = \beta(u_{2n+1} + u_{2n-1} - 2u_{2n}) \\ m_2 \dfrac{\partial^2 u_{2n+1}}{\partial t^2} = -\beta(u_{2n+1} - u_{2n}) + \beta(u_{2n+2} - u_{2n+1}) \\ \qquad\qquad = \beta(u_{2n+2} + u_{2n} - 2u_{2n+1}) \end{cases} \tag{1.5}$$

and searching for solutions of Eq.(1.6) in the form:

$$\begin{cases} u_{2n}(t) = A \exp i(k(2n)a - \omega t) \\ u_{2n+1}(t) = B \exp i(k(2n+1)a - \omega t) \end{cases} \tag{1.6}$$

where A and B represent amplitude terms. These equations can be rewritten in matrix form as:

$$\begin{bmatrix} (2\beta - m_1\omega^2) & -2\beta cos(ka) \\ 2\beta cos(ka) & -(2\beta - m_2\omega^2) \end{bmatrix} \begin{bmatrix} A \\ B \end{bmatrix} = \begin{bmatrix} 0 \\ 0 \end{bmatrix} \tag{1.7}$$

Equations (1.7) admit non-trivial when the determinant of the matrix is equal to 0:

$$\omega^4 - 2\beta \left(\frac{m_1 + m_2}{m_1 m_2} \right) + \frac{4\beta^2 sin^2(ka)}{m_1 m_2} = 0 \tag{1.8}$$

from which we can obtain the circular frequency as:

$$\omega(k) = \sqrt{\beta \frac{m_1 + m_2}{m_1 m_2} \left(1 \pm \sqrt{1 - 4\frac{m_1 m_2 sin^2(ka)}{(m_1 + m_2)^2}} \right)} \tag{1.9}$$

Eq.(1.9) has two real solutions: $\omega_-(k)$ and $\omega_+(k)$, both with periodicity π/a in k. The first Brillouin zone ranges from $-\pi/2a$ to $\pi/2a$. It is worth noting that the first Brillouin zone is halved in size due to the chain's direct lattice having twice the unit cell size of a monoatomic chain.
In Figure 1.3 it is shown the dispersion relation within the irreducible Brillouin zone (with k values moving from 0 and $\pi/2a$) as a function of the ratio m_2/m_1 when it is greater than or equal to 1.

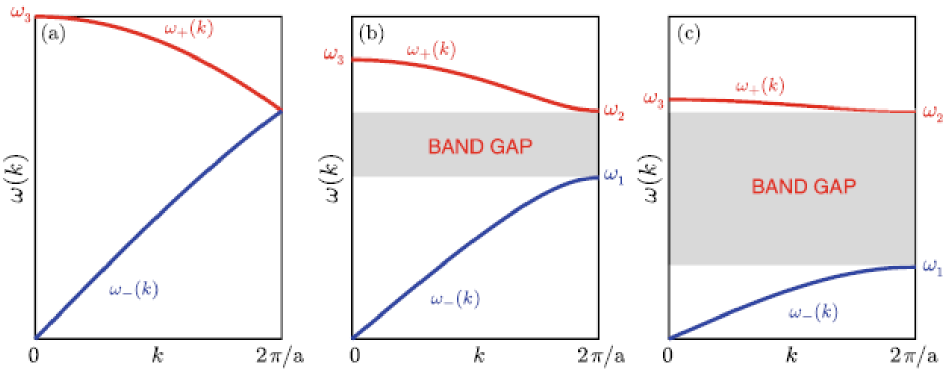

Figure 1.3: Dispersion relation in the irreducible BZ of the investigated structure. Three cases are represented: a) $m_2 = m_1$, b) $m_2 = 2m_1$ and c) $m_2 = 10m_1$

It can be observed that when $m_2 = m_1$, the dispersion relation aligns with that of an infinite monoatomic chain but is confined within a smaller irreducible

Brillouin zone. Additionally, as the mass ratio increases, a band gap appears at the boundary of the Brillouin zone, and the size of the gap increases proportionally with the mass ratio.

1.1.2 Crystallography elements

Knowledge of crystallography is essential to understanding how acoustic waves interact with periodic structures. The first fundamental concept in solid state physics is the *Bravais lattice*, also referred to as direct lattice, which is defined in Ref[3] as: *all points with position vectors R of the form*

$$R = n_1\boldsymbol{a_1} + n_2\boldsymbol{a_2} + n_3\boldsymbol{a_3} \tag{1.10}$$

where $\boldsymbol{a_1}$, $\boldsymbol{a_2}$ and $\boldsymbol{a_3}$, are any three vectors not all in the same plane, and n_1, n_2 and n_3 range through all integral values. Thus the point $\sum n_i\boldsymbol{a_i}$ is reached by moving n_i steps of length a_i in the direction $\boldsymbol{a_i}$ for $i = 1{,}2$ and 3. Where the vectors $\boldsymbol{a_i}$ are called *primitive vectors* and they represent the shortest linearly independent vectors that can be used to recreate the entire lattice structure by translation. As a consequence, it is possible to define the *primitive cell.* This is the smallest repeating unit found within a crystal lattice that can be used to recreate the whole lattice structure through translations. The primitive cell contains only one lattice point and is the fundamental building block of the crystal's structure.

The primitive cells are selected in such a way that they possess the same translational symmetry as that of the entire crystal lattice. However, the selection of primitive vectors to describe the unit cell is not unique, which in turn makes the primitive cell selection not unique too. Therefore, the most commonly used solution for selecting the primitive cell is the Wigner-Seitz cell. This particular volume is defined around a single lattice point and contains all the closest points to it. It is possible to define this volume around a single lattice point by connecting it to all other points in the lattice and drawing lines between them (in blue in Fig.1.4), then taking the smallest polyhedron bounded by the planes bisecting those lines (in red).

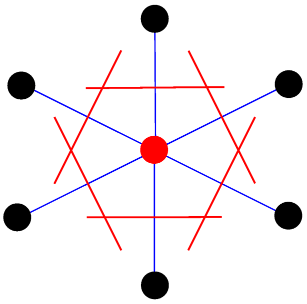

Figure 1.4: Wigner-Seitz cell

1.1.3 Reciprocal lattice and Irreducible Brillouin Zone

As we saw in the previous section, the direct lattice is defined in real space, but an equally important definition is the reciprocal lattice. In the direct lattice a periodic function $f(\vec{r})$ follow the condition $f(\vec{r}) = f(\vec{r} + \vec{R})$ where $R = l\vec{a}_1 + m\vec{a}_2 + n\vec{a}_3$. This periodic function, which is $\vec{R} - periodic$, can be expressed using Fourier series:

$$f(\vec{r}) = \sum_{\vec{G}} f(\vec{G}) e^{i\vec{G}\cdot\vec{r}} \tag{1.11}$$

where $\vec{G}$ are the *reciprocal lattice vector* and $f(\vec{G})$ are the Fourier coefficients of $f(\vec{r})$. This allows us to write:

$$f(\vec{r} + \vec{R}) = \sum_{\vec{G}} f(\vec{G}) e^{i\vec{G}\cdot(\vec{r}+\vec{R})} = \sum_{\vec{G}} f(\vec{G}) e^{i\vec{G}\cdot\vec{r}} \tag{1.12}$$

From Eq.1.12 we can conclude that $e^{i\vec{G}\cdot\vec{R}} = 1$, which is true when:

$$\vec{G} \cdot \vec{R} = 2\pi \cdot N; \ N \in \mathbb{Z} \tag{1.13}$$

Therefore, the reciprocal lattice can be defined as the points whose positions are given by a set of vectors $\vec{G}$ satisfying the condition in Eq.1.13 for $\vec{R}$ in the Bravais lattice. Being $\vec{R}$ a linear combination of primitive vectors $\vec{a_i}$ with $i = 1,2,3$, we can describe also $\vec{G}$ as linear combination of basis vector $\vec{b_i}$, $i = 1,2,3$. and so we could write:

$$\vec{G} = l'\vec{b_1} + m'\vec{b_2} + n'\vec{b_3} \tag{1.14}$$

where l', m' and n' and $\vec{b_i}$ are not defined yet.
By explicating $\vec{R}$ and $\vec{G}$ inside Eq.(1.13) and imposing the basis $\{\vec{b_i}\}$ orthonormal to the basis $\{\vec{a_i}\}$ and writing $\vec{b_i} \cdot \vec{a_j} = 2\pi\delta_{ij}$ where δ_{ij} is the Kronecker's delta. We obtain:

$$l'l + m'm + n'n = N \tag{1.15}$$

Being $N \in \mathbb{Z}$ means that the left-hand side of Eq.(1.15) need to be an integer, therefore $l', m', n' \in \mathbb{Z}$ too. As a consequence, a reciprocal lattice is also a Bravais lattice.
We can then start from $\vec{b_1}$ to define $\vec{b_i}$. Considering that $\vec{b_1} \perp \vec{a_2}$ and $\vec{b_1} \perp \vec{a_3}$, we can write $\vec{b_1} = \lambda \cdot \vec{a_2} \times \vec{a_3}$ where λ is an unknown constant. Moreover, $\vec{a_1} \cdot \vec{b_1} = 2\pi = \lambda\vec{a_1} \cdot (\vec{a_2} \times \vec{a_3})$ from which we can obtain $\lambda = \frac{2\pi}{\vec{a}_1\cdot(\vec{a}_2\times\vec{a}_3)}$. A similar deduction can be proved for vector $\vec{b_2}$ and $\vec{b_3}$. Considering also that $\vec{a}_1 \cdot (\vec{a}_2 \times \vec{a}_3) = \vec{a}_2 \cdot (\vec{a}_3 \times \vec{a}_1) = \vec{a}_3 \cdot (\vec{a}_1 \times \vec{a}_2)$, the basis vectors of the reciprocal lattice can be written as function as the basis vectors of the direct lattice as:

$$\vec{b_1} = 2\pi \frac{\vec{a}_2 \times \vec{a}_3}{\vec{a}_1 \cdot (\vec{a}_2 \times \vec{a}_3)} \tag{1.16a}$$

$$\vec{b}_2 = 2\pi \frac{\vec{a}_3 \times \vec{a}_1}{\vec{a}_1 \cdot (\vec{a}_2 \times \vec{a}_3)} \tag{1.16b}$$

$$\vec{b}_3 = 2\pi \frac{\vec{a}_1 \times \vec{a}_2}{\vec{a}_1 \cdot (\vec{a}_2 \times \vec{a}_3)} \tag{1.16c}$$

The scalar value $\vec{a}_1 \cdot (\vec{a}_2 \times \vec{a}_3)$ in Eq.(1.16) represents the volume of the unit cell because is the volume of the parallelepiped formed by the three primitive vectors $\{\vec{a}_i\}$ of the original direct lattice. It's worth noting that the magnitude of the reciprocal lattice vectors is inversely proportional to the magnitude of the direct lattice vectors. This relationship is the reason why it's called the *reciprocal lattice*.

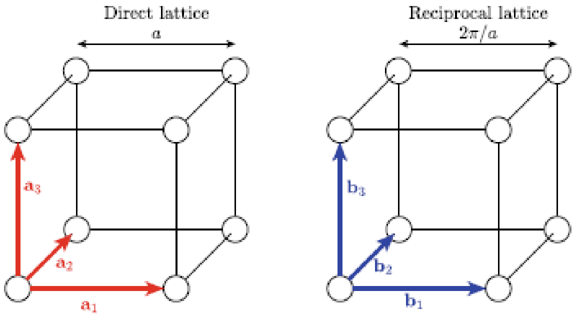

Figure 1.5: On the left side, a cubic lattice, while on the right side, its reciprocal lattice [4]

Since the reciprocal lattice is a Bravais lattice, one can determine its Wigner-Seitz cell, which, in the reciprocal space, is commonly referred to as *First Brillouin Zone*. Moreover, in the reciprocal lattice, the planes that intersect the lines connecting a specific point to all the other points are referred to as *Bragg planes*. Consequently, the First Brillouin Zone can be thought of as the set of all points in reciprocal space that you can reach from the origin without encountering any Bragg planes. The smallest possible Brillouin zone is called the *irreducible Brillouin zone*.

1.2 Topological States

The quantum Hall effect (QHE) was discovered by Von Klitzing in 1980 [5] when he proved the existence of an electron gas sample showing a quantized conductivity independently from its size and from impurities. This discovery created a breakthrough in the description that condensed-matter physics had always used regarding the distinctive phase of matter. A few years later, it was demonstrated [6][7] that this phenomenon is characterized by a unique classification model based on the concept of topological order. This means that the phase of matter goes beyond symmetry breaking, implying that two distinct phases can possess the same symmetry.
This description of matter's phase topology has significant implications for its fundamental properties. These properties remain unchanged under continuous material perturbations and only alter during quantum phase transitions, like the Hall conductance in the study of Klitzing. The quantization we observe is a result of non-trivial topological properties in the energy bands. These properties are distinguished by the Chern number, as outlined in the TKNN theory [7]. The Chern number is a non-zero topological invariant that describes the geometric phase, also known as the Berry phase, accumulation throughout the Brillouin zone. This means that the Chern number is strongly connected to the energy bands in the momentum space.

In classical insulators, the Chern number is equal to zero. However, in topological non-trivial systems, a Chern number different from zero is produced. This results in the generation of an electronic property where the bulk is insulating, while conduction is present on the edge. This can be observed through the appearance of a gapless edge state in the bulk energy gap. The discovery of certain properties was made possible through the application of magnetic fields. It was later discovered that non-trivial topological phases could be generated through the spin-orbit coupling of a material. These phenomena are known as the quantum spin Hall effect (QSHE) and one of the first examples was observed by Kane et al. with graphene [8]. In a system featuring spin-orbital coupling, a pair of gapless edge states emerge within the insulating band gap. These edge states carry conjugate electronic spins and display spin-dependent propagation behaviors. Furthermore, the total Hall conductance and the Chern number are equal to zero, indicating that the time-reversal symmetry is preserved. It is precisely the time-reversal symmetry that safeguards the spin-dependent edge states.

The quantum valley Hall effect (QVHE) proposes a new way for a topological state to manifest itself by introducing a discrete degree of freedom, known as the "valley" [9]. This term refers to the two energy extrema in the band structures in momentum space. At these two points, the Berry curvature has an opposite sign, which means that the value of its integral over the entire Brillouin zone is zero, while within each valley it is non-zero. This creates a valley-selective topologically non-trivial property in the system. What's interesting is that, in this case, the time-reversal symmetry is preserved. Although these topological phases differ in nature, they all share a common characteristic: the edge states span the bulk band gap and separate domains with different Chern numbers.

1.2.1 Acoustic valley Hall effect

The discrete-valley degree of freedom, which characterizes quantum states associated with energy extrema in the k-space, has garnered considerable attention due to its possibility of being a novel information carrier, not too dissimilar to spin in spintronics. The idea of bringing the valley concept to classical wave system brought scientists to demonstrate the creation of valley-like frequency dispersions in artificial crystals, both with photonic crystals[10] and sonic crystals[11]. Shortly thereafter, the theoretical prediction and experimental observation of the quantum valley Hall effect (QVHE) and the corresponding valley-protected edge state were achieved in two-dimensional acoustic systems [12].

The quantum valley Hall effect is different from the quantum Hall effect and the quantum-spin Hall effect. Unlike the latter two, the QVHE does not rely on intricate mechanisms to achieve TRS breaking but instead relies on the breaking of space inversion symmetry (SIS) while preserving time-reversal symmetry (TRS). This makes QVHE more feasible for practical applications. However, this also means that QVHE is a less robust phenomenon, sometimes called a "weak" topological effect. It is worth noting that despite sharing similar lattice structure design principles, these phenomena, which do not involve quantum mechanical effects, are named the "acoustic valley Hall effect" (AVHE).

1.2.2 Topological materials for Valley Hall Effect

As mentioned above, the valley Hall effect in acoustic systems exhibits an analogous effect to QVHE whiteout involving actual quantum mechanical behavior. In order to obtain topological properties based on the valley Hall mechanism some prerequisites are necessary [13].

To design a material with topological properties, the first step is to determine a lattice structure with specific dispersion characteristics. In particular, the band structure should feature linear, i.e. isotropic, dispersions originating from a degenerate point, named *Dirac Point* (DP), while the linear branches forming a conical structure in the 3D space of wavevector and frequency $[kx, ky, \omega]$ are referred to as the *Dirac Cone* (DC). In order to have topological properties based on the valley Hall mechanism, this Dirac cone should be positioned at the boundary of the Brillouin zone, as shown in Fig.1.6.

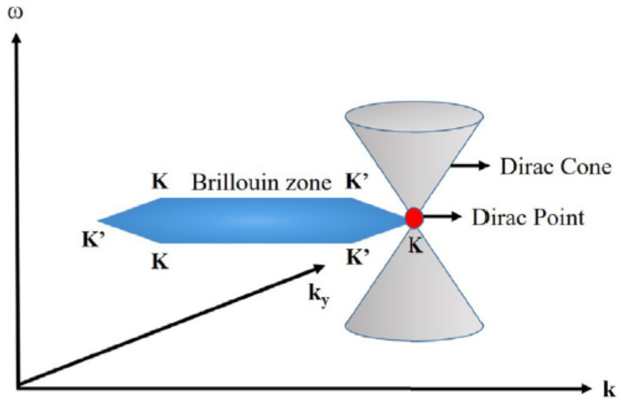

Figure 1.6: Dirac dispersion at the boundary of the Brillouin zone in momentum space. Picture from [13]

It is worth noting that different classes of topological properties could also be derived from Dirac cones located at the center of the Brillouin zone [14]. Importantly, the presence of such dispersion properties is guaranteed for specific lattice configurations with particular symmetries, making these dispersion properties symmetry-protected.

Opening a frequency bandgap is the second crucial step toward in constructing VHE-based materials. To achieve this, it is necessary to lift the degeneracy at the Dirac Point, which can be done by breaking the space inversion symmetry of the original lattice. This solution results in gapped band structures around the valleys, along with the separation of the originally degenerate modes forming the Dirac Cones. Space inversion symmetry breaking is proved to be possible through either permanent changes [15] or temporarily induced deformation [16]. The application of anti-symmetric perturbations (positive and negative deformation with the same type and amplitude, for example) results in band structures having a topological charge around valleys with opposing signs. This topological charge, an invariant characterizing the lattice's nature concerning the topology of its band structure, implies that the two lattices are topologically distinct after space inversion symmetry breaking. These distinct lattices can be referred to as the material's two separate (topological) *phases*.

The third and last element necessary to achieve topological properties involves assembling a lattice structure where the two phases contrast to form a physical interface, known also as *domain wall*. Therefore, the valley topological charge undergoes a transition across this physical interface, progressing from positive to zero and then to negative (or vice-versa). Considering the meaning of the topological charge, this behavior implies that the topological band-gap will close and reopen when crossing the interface, developing distinct topological significance. Considering the revealed connection of the edge states to bulk topological properties[17], when the discrepancy in topological invariants between the material phases constituting the domain walls is different from zero, the wall will sustain edge states localized at the interface and topologically protected against disturbance.

Chapter 2

Counter mode resonator for purely longitudinal modes

2.1 CMR - Contour Mode Resonators

AlN FBAR resonators have been the leading choice for a long time due to their high-quality factor, Q, and electromechanical coupling coefficient k_t^2. However, the main limitation of these resonators is that their resonant frequency is fixed once the film thickness has been chosen since:

$$f_{res} = \frac{1}{2h}\sqrt{\frac{C_{33}}{\rho}} \tag{2.1}$$

where C_{33} comes from the piezoelectric coefficient, h is the thickness of the piezoelectric layer and ρ its density.

In spite of the availability of some solutions such as trimming or mass loading for tuning the frequency of an FBAR device, a new type of resonator called the Counter Mode Resonator (CMR) has been developed to overcome this issue. These resonators utilize the vertical field to create displacement in the lateral direction via the S_0 Lamb-Wave mode. They also offer the ability to tune the resonance frequency by adjusting the width of the piezoelectric plate.

Fig.2.1 shows a typical configuration of this laterally vibrating piezoelectric resonator, which is formed by a thin piezoelectric film in between two metallic electrodes. These two metallic layers allow the application of a potential across the thickness of the film in between which results in a lateral strain through the device's plane. When the frequency of the signal that causes excitation aligns with the mechanical resonance of the piezoelectric body, the amplitude of vibration increases significantly. This amplified vibration is then converted into an electrical

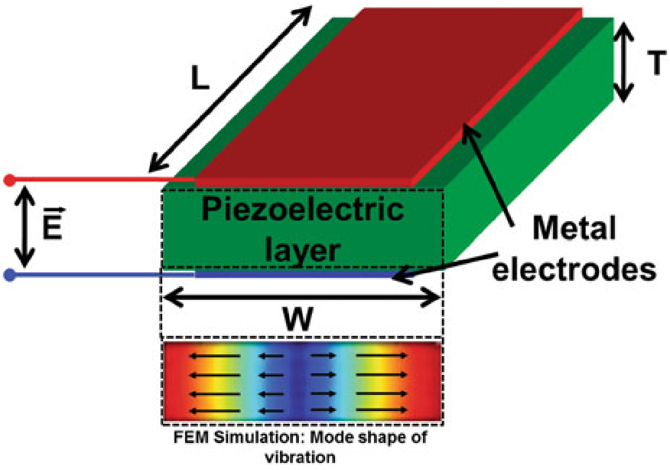

Figure 2.1: Schematic illustration of CMR [18]

signal via the direct piezoelectric effect. Consequently, a change in the magnitude of displacement is produced.

To define the modes and the resonant frequency of the CMR, one can employ the a solution to the wave equation with appropriate boundary conditions. For a longitudinal resonator oscillating along its width, the wave equation in one dimension of the space can be expressed as:

$$\rho \frac{\partial^2 u}{\partial t^2} = E_p \frac{\partial^2 u}{\partial x^2} \tag{2.2}$$

Here, E_p is the equivalent Young's modulus and ρ the equivalent density of the material stack defining the device. u is the displacement, x the single dimension of the space corresponding to the direction of the vibration, and t is the time. One general solution to this equation can be written as:

$$u(x,t) = [a \sin(\beta x) + b \cos(\beta x)] e^{j\omega_0 t} \tag{2.3}$$

We assume, as boundary conditions, no stress and stress gradient at $x = \pm W/2$. Therefore we obtain from 2.3:

$$u(x,t) = U(x)X(t) = \sin(\beta_n x) e^{j\omega_0 t} \tag{2.4}$$

$$\beta_n = (2n-1)\frac{\pi}{W} \tag{2.5}$$

Finally, the resonance frequency can be found by substituting Eq.2.4 in Eq.2.2. The vibrational frequency of the fundamental mode can be found by setting $n = 1$ in the solution computation:

$$f_0 = \frac{1}{2W}\sqrt{\frac{E_q}{\rho}} \tag{2.6}$$

As previously mentioned, the expression of f_0 clearly shows that the main characteristic of CMRs is the resonance frequency of the resonator being defined by its lateral geometric dimension. This is an important quality because it allows for the lithographic definition of multiple frequency devices on a single substrate, unlike the FBAR. Hence, components can be produced that can function across a wide spectrum, independent of the piezoelectric structure's thickness or length. This provides greater freedom in the resonator design as the thickness and length can be adjusted to define its electrical static capacitance C_0 and, consequently, its impedance.

2.1.1 BVD model

The resonance that a piezoelectric resonator generates when one of its acoustic modes is excited can be detected as a variation in its input admittance. A very useful and simple circuital model often used to describe and characterize one port acoustic resonator is the so-called Butterworth-Van Dyke (BVD) model.

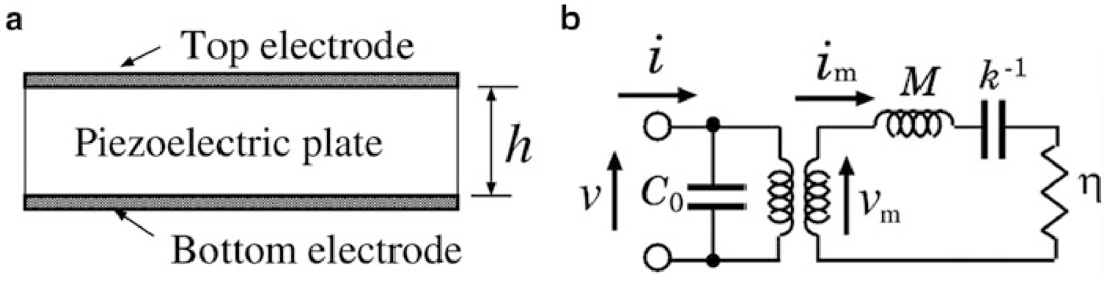

Figure 2.2: (a) The physical model of a BAW resonator. (b) The electromechanical equivalent circuit

To define this model, it is possible to start from a simple BAW resonator as the one depicted in Fig.2.2(a). Here, when a sinusoidal voltage ν is applied at the electrodes with frequency f, due to the piezoelectric effect, a mechanical force ν_m is generated and, as a consequence, the piezoelectric layer is subjected to a displacement u. The relation that undergoes between these phenomena can be written as:

$$\nu \propto \nu_m = M\frac{d^2u}{dt^2} + \nu\frac{du}{dt} + Ku \tag{2.7}$$

where ν is the effective viscosity characterizing the plate, M its effective mass and K the effective spring constant. From the dumped oscillating system point of view, the right-hand side of equation 2.7, the three terms can correspond to inertia, friction, and elasticity, respectively.

Considering the reciprocity of the piezoelectric effect, the electrical charges q_m induced on the electrodes will be proportional to u. Therefore, we can design the equivalent electromechanical circuit shown in Fig.2.2(b) where $i_m = du/dt$ is a mechanical current, and clamped capacitance C_0 is used to express the electrostatic coupling between the electrodes. [18]

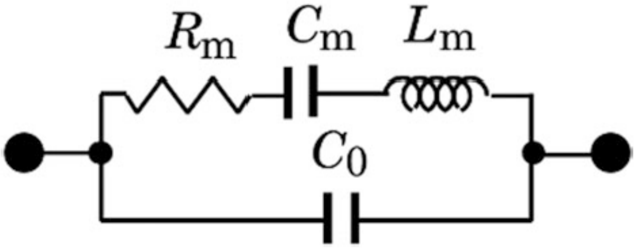

Figure 2.3: Butterworth-Van Dyke (BVD) model

When only the electrical characteristics are taken into account, the equivalent circuit from before can be reduced to the Butterworth-Van Dyke (BVD) model shown in Fig.2.3, where the motion resistance, capacitance, and inductance are denoted with R_m, C_m and L_m, respectively.

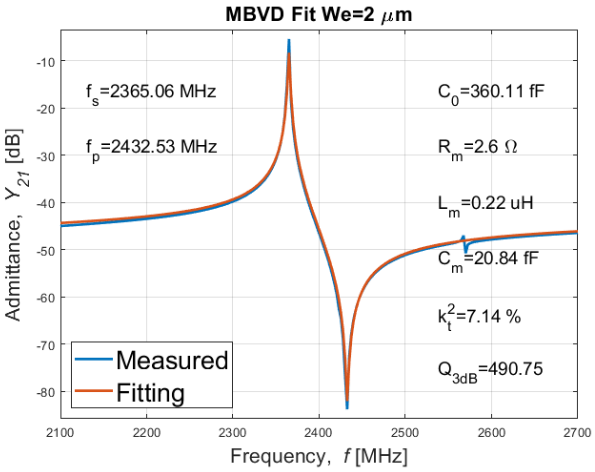

Figure 2.4: An example of BVD model fitting of a resonator's FEM simulation

Fig.2.4 shows the example of the electrical parameters obtained from the BVD fitting of an admittance response extracted from a FEM simulation of a resonator. From the BVD model one can express the admittance Y as:

$$Y = 2\pi j f C_0 \frac{1 - \left(f/f_a\right)^2 + j\left(f/f_a\right) Q_a^{-1}}{1 - \left(f/f_r\right)^2 + j\left(f/f_r\right) Q_r^{-1}} \tag{2.8}$$

where f_r is defined as the resonance frequency where the series resonance occurs and, from the equivalent circuit, it results equal to:

$$f_r = \frac{1}{2\pi\sqrt{L_m C_m}} \tag{2.9}$$

while when the parallel resonance occurs at the anti-resonance frequency f_a:

$$f_a = \frac{1}{2\pi\sqrt{\frac{L_m}{C_m^{-1}+C_0^{-1}}}} \tag{2.10}$$

Also in Eq.2.8 the resonance and anti-resonant quality factor appears and they are, respectively:

$$Q_r = \frac{2\pi f_r L_m}{R_m} \tag{2.11}$$

and

$$Q_a = \frac{2\pi f_a L_m}{R_m} \tag{2.12}$$

Moreover, with the definition of the electromechanical coupling coefficient k_t^2 is possible to rewrite the the parameters as:

$$C_m = \frac{8 C_0 k_t^2}{\pi^2} \tag{2.13}$$

$$L_m = \frac{1}{\omega^2 C_m} \tag{2.14}$$

$$R_m = \frac{\omega_r es L_m}{Q_r} \tag{2.15}$$

2.1.2 Figure of Merit of a Resonator

A resonator based on piezoelectric principles functions as an electromechanical device wherein electrical and mechanical energies undergo reciprocal conversion at a resonance frequency. This coupling stems from the interaction between stress and electric field within a piezoelectric material. Furthermore, on each vibrational half cycle, both the mechanical and the applied electrical energy undergo from a potential to a kinetic conversion and back. Consequently, the overall effectiveness of a resonant system is strictly connected to the efficiency of these two mechanism. Two specific parameters are defined to assess the efficiency of these energy conversions within a resonator: the electromechanical coupling factor (k_t^2) and the quality factor (Q).

Quality Factor - Q

The quality factor is a measure of energy lost in a resonator. It is specifically connected to the energy that directly escapes or cannot be stored after a transformation, such as heat. Therefore, a general definition of Q is [19]:

$$Q = 2\pi \frac{Peak\, energy\, stored}{Energy\, dissipated\, per\, cycle} \tag{2.16}$$

Where the overall quality factor Q_{tot} of the resonator can be found considering all the different dissipation mechanisms inside it:

$$Q_{tot} = 2\pi \frac{E_{stored}}{\sum_i E_{dissipated_i}/cycle} = \left(\sum_i \frac{1}{Q_i}\right)^{-1} \tag{2.17}$$

A comparable description of Q can also be given considering a damped mass-spring system governed by the differential equation $M\ddot{x} + C\dot{x} + Kx = 0$:

$$Q = \frac{1}{2\zeta} \tag{2.18}$$

From Eq.2.18 it is possible to notice that Q is inversely proportional to the dumping ratio ζ, which is defined as C divided by the value of the critical damping C_c [20]. Nevertheless, a more convenient definition to write Q is the one based on the parameters present on the frequency response plot, which is more used for the characterization of resonators:

$$Q = \frac{f_0}{BW_{3dB}} \tag{2.19}$$

where f_0 is the resonance frequency and BW_{3dB} bandwidth is the width of the range of positive frequencies where the admittance peak is attenuated by $3dB$. A resonator that has a higher quality factor (Q) will exhibit a more sharp resonance.

Electromechanical coupling coefficient - k_t^2

The coupling factor serves as a metric for assessing the effectiveness of the conversion between the electrical and mechanical domains and vice versa. An essential consideration in its analysis is distinguishing between the electromechanical coupling factor characteristic of the resonator and the coupling factor intrinsic to the material itself. The latter remains independent of the resonator design, while the former can be enhanced or diminished based on the implementation of electrodes. The piezoelectric coupling factor, denoted as K^2, can be defined in a lossless scenario as:

$$K^2 = \frac{W_M}{W_M + W_E} \tag{2.20}$$

where W_M is the work delivered by a piezoelectric actuator to a mechanical load when the former is preloaded with a potential energy of $W_M + W_E$ [18]. This means that K^2 is the upper limit for the efficiency of energy conversion in a resonator made by a certain piezoelectric material.

For a piezoelectric resonator with a given geometry, the effective electromechanical factor is used to quantify its conversion efficiency, and it is commonly expressed as:

$$k_{eff}^2 = \frac{f_p^2 - f_s^2}{f_p^2} \tag{2.21}$$

with f_s and f_p, the resonance and anti-resonance frequencies, respectively. However, another slightly different but common definition of the electromechanical coupling factor is also used [21]:

$$k_{eff}^2 = k_t^2 = \frac{\pi^2}{8} \frac{f_p^2 - f_s^2}{f_s^2} = \frac{\pi^2}{8} \frac{C_m}{C_0} \tag{2.22}$$

Finally, a standard definition of the *Figure of Merit* (FoM) of a piezoelectric resonator is then defined as:

$$FoM = \frac{k_t^2 \cdot Q}{1 - k_t^2} \tag{2.23}$$

which can be simplified for small values of k_{eff}^2 as:

$$FoM = k_t^2 \cdot Q \tag{2.24}$$

The significance of this FoM in assessing a resonator's performance becomes clear when one considers that a higher coupling factor implies an efficient conversion of electrical to mechanical energy. Simultaneously, a larger Q value indicates a weaker coupling between the system's energy and undesired forms of fluctuating energy. Consequently, greater coupling and Q directly contribute to an improved SNR.

2.2 Acoustic Metamaterials

In recent years, there has been a surge of interest and research focus on designing and developing acoustic metamaterials aimed at tailoring the propagation of acoustic waves[22][23][24]. These engineered materials, known as phononic or acoustic metamaterials, exhibit unique properties that go beyond those found in conventional materials. One of the key objectives in this field is the creation of structures that can effectively control the transmission, reflection, and manipulation of acoustic waves across a broad frequency range.

Of particular interest is the exploration of acoustic metamaterials that feature stopbands and passbands—frequency ranges where the transmission of acoustic waves is selectively inhibited or permitted. These distinct acoustic band structures are engineered through careful design of the unit cell geometry, arrangement of constituent elements, and material properties. The ability to create stopbands, where certain frequencies are forbidden, and passbands, where others are allowed, opens up new possibilities for unprecedented control over acoustic wave propagation.

2.2.1 Two dimensional resonant rods - 2DRR

A solution to exploiting the possibility of acoustic metamaterial is the 2D-resonant-rods (2DRR) proposed by Zhao [25][26], where a layer of AlN is partially etched in order to obtain a series of resonant piezoelectric rods. While the top electrodes separately cover each rod, the uniform bottom electrode allows the Aluminum Nitride layer to have an optimal crystal orientation.

Figure 2.5: Schematic of a 2DRR device made by 6 unit cells

This particular design allows the confinement of the resonant vibration within the rods, as shown in Fig.2.6a, by minimizing the coupling between adjacent rods because the steep trenches display an evanescent lateral wavevector component at f_{res}. Additionally, the design of the trenches prevents the formation of any electrical field lines that may be generated between the top electrode grating, resulting in an increment of k_t^2 with respect to similar devices such as 2DMRs and CLMRs.

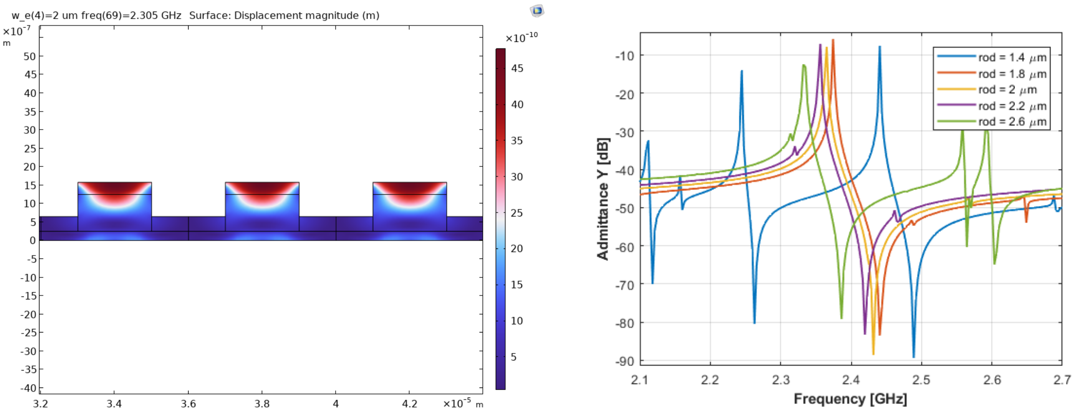

(a) FEM simulated resonant total displacement of a 2DRR.

(b) Frequency response of the 2DRR for different rod width

Figure 2.6:

A parameter of particular importance in the 2DRR's performance is the width of the rod. The rod width plays a crucial role in determining various aspects of the device's functionality and overall efficiency, such as the resonance frequency, f_{res}, and the electromechanical coupling coefficient k_t^2. Figure 2.6b illustrates the frequency response, as determined through finite element method (FEM) simulations, of a two-dimensional resonator array (2DRR) formed by 20 unit cells. The lower platinum electrode has a thickness of 250 nm, and the upper aluminum electrode is 330 nm. The rods are elevated by 6 nm above the "first" AlN layer, which itself has a thickness of 400 nm.

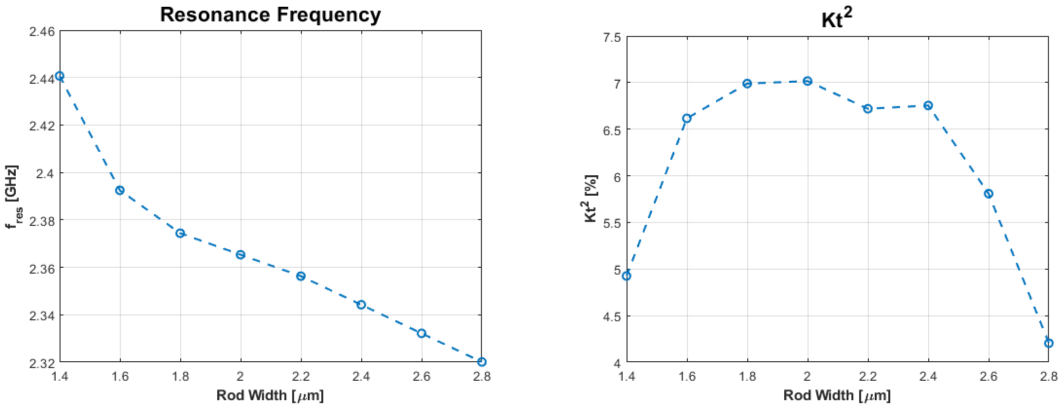

(a) Resonance frequency vs rod width

(b) k_t^2 vs rod width

Figure 2.7: Variation of the resonance frequency and the k_t^2 at different values of the rod width

It is understandable that as the width of the rod deviates significantly from $2\mu m$, achieving well-separated resonant modes becomes increasingly challenging. Also, as illustrated in Figure 2.7b, it is evident that the k_t^2 value diminishes noticeably when the rod width deviates significantly from that value. Nevertheless, the adjustment of the rod width enables a reasonably efficient control over the resonance frequency, which decreases with the incremental widening of the rod, as depicted in Figure 2.7a.

Another noteworthy outcome of the investigation of the two-dimensional resonant rods device is the identification of distinct stopband and passband phenomena occurring at varying frequencies. The analytical analysis of these phenomena is illustrated in Figure 2.8. The resulting transmission coefficient T clearly indicates the emergence of a stopband in mode propagation, attributed to the impact of a large and evanescent wavevector that restricts the exchange of acoustic energy between adjacent unit cells [25].

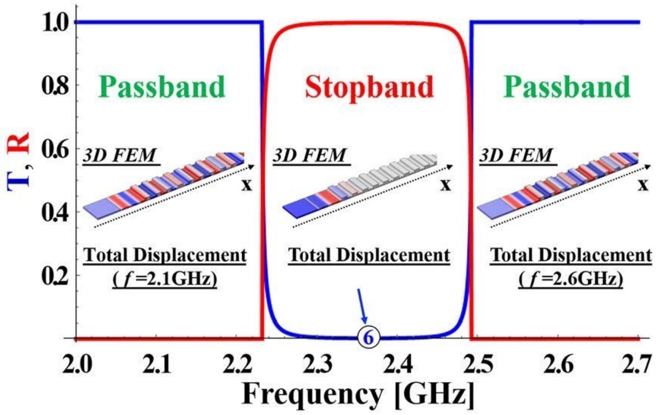

Figure 2.8: Analytical trend of the Trasmission T, in blue, and reflection R, in red, vs frequency from [25]

Chapter 3

Unit Cell Bloch Diagram

3.1 Unit cell simulation

In this study, we examine a one-dimensional topological system based on the well-known Su-Schrieffer-Heeger (SSH) model [27]. This model is widely considered the most straightforward configuration that sustains a topologically nontrivial bandgap. The idea behind this model is to alternate pairs of elements with higher or lower coupling strength in order to create a discontinuity where we can observe the generation of a topological-protected edge state. We achieve this by using a piezoelectric metamaterial derived from the 2DRR, composed of a substrate of AlScN with periodically spaced rods placed above it.

3.1.1 Definition of the simulation model

To achieve our goal, we thoroughly analyzed the band structure of the unit cell of our metamaterial. The idea was to achieve a symmetric band structure, that was possible by designing a symmetric unit cell. In order to do so the rods componing the device are placed in symmetrically respect the middle point of the unit, so given a cell of length U and the rods of equal thickness R, their distance to respect to the edges of the unit cell T was defined as $T_0 = (U/2 - R)/2$. The result is the perfectly symmetric unit cell named $A0$, shown in Fig.3.1.

In order to numerically compute the dispersion relation of the unit cell, the finite element method (FEM) was used by the application of the *Floquet boundary conditions*. These boundary conditions are frequently used to extract the dispersion relation of metamaterials or other periodic architectures. Usually, the Floquet boundary condition can be expressed as:

$$p_{t,dst} = p_{t,src} e^{-i\boldsymbol{k}_F(\boldsymbol{r}_{dst} - \boldsymbol{r}_s rc)} \tag{3.1}$$

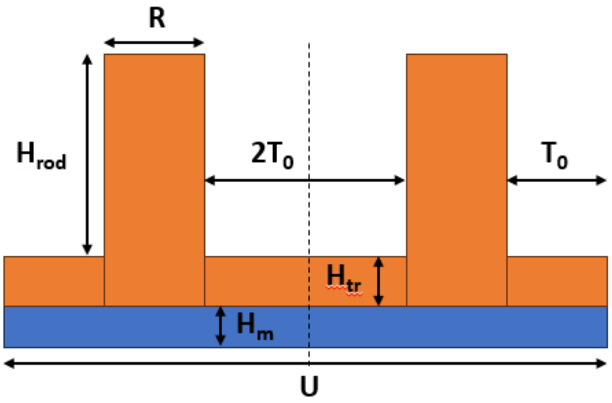

Figure 3.1: Unit cell

Here, the sweep of the wavevector k_F is defined by the user, and the coordinates where the BC are applied are defined by $\boldsymbol{r}_{src}$ and $\boldsymbol{r}_{dst}$: the source and the destination edges of the cell respectively [28].

In this work, we used the Pressure Acoustic module of COMSOL Multiphysics to build our unit cell and applied the Floquet boundary conditions to its parallel lateral edges. Through the FEM method, we solve in the frequency domain the inhomogeneous Helmholtz equation:

$$\nabla \cdot \left(-\frac{1}{\rho_c} \left(\nabla p_t - q_d \right) \right) - \frac{k_{eq}^2 p_t}{\rho_c} = Q_m \tag{3.2}$$

where $p_t = p_b + p_s$ is the total pressure, which is the sum of the scattered field p_s, and the background pressure p_b, which was set to be equal to 0. k_{eq} is the wave number and can be written as:

$$k_{eq}^2 = \left(\frac{\omega}{c_c} \right)^2 - k_z^2 \tag{3.3}$$

where k_z is the *out-of-plane* wave-number and it is set to be equal to 0, while the speed of sound in the material is defined as:

$$c_c = \sqrt{\frac{K}{\rho_c}} \tag{3.4}$$

where K and ρ_c are the *bulk modulus* and the *density* of the material, respectively. In order to solve the eigenvalue problem, Eq.3.2 is written in its eigenfrequency formulation, where the source terms are absent, as:

$$\nabla \cdot \left(-\frac{1}{\rho_c} \right) + \frac{\lambda^2 p}{\rho_c c_c^2} = 0 \tag{3.5}$$

λ is the eigenvalue and it is related to the frequency f, as well as to the angular frequency ω, being $\lambda = i2\pi f = i\omega$. Therefore, the eigenvalues are evaluated by sweeping the wavenumber k. The dispersion curves are then obtained by plotting the frequency versus the wavenumber or vice-versa.

3.1.2 Unit Cell Analysis

In order to attain the Dirac cones, we design the unit cell to be the symmetric repetition of a starting *mono-rod* cell as the one depicted in Fig.3.2. The result is the unit cell with a lattice constant, U, which is two times the one, u, of the mono-rod cell, while all other geometric parameters remain the same [29].

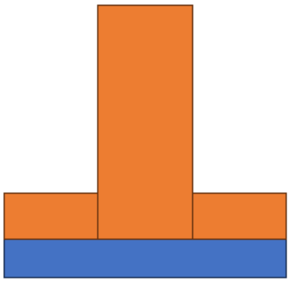

Figure 3.2: Structure of the mono-rod cell

As mentioned in chapter 1, the first Brillouin zone is strongly dependent on the lattice constant. This is because the value of k_x is periodic within the range of $-\pi/U$ and π/U. Therefore, the dimension of the first Brillouin zone of the unit cell will be exactly half of the Brillouin zone of the half-cell since $U = 2u$, as it is possible to see from Fig.3.3:

Based on the observation in Fig.3.3b, it is apparent that the reduced dimension of the Brillouin zone leads to a phenomenon known as *band folding*. This results in the bending of the dispersion curves of the original half-cell, as displayed by the red dots in the figure. In fact, when these curves reach the edge of the "new" Brillouin zone, they fold on themselves and create a Dirac point.

The variation in the total length of the unit cell can serve as an important tuning parameter for the cell. As shown in Fig.3.4, the frequency distribution of the cell's bands is strongly dependent on the value of U. When the first Brillouin zone expands, i.e. for smaller U, the distances between band gaps increase, resulting in higher frequency dispersion bands.

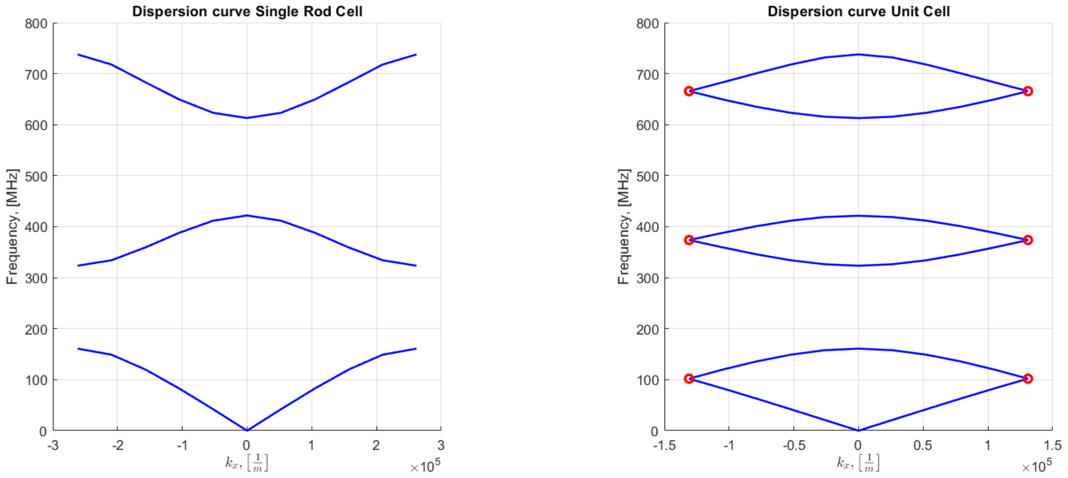

(a) Dispersion curve of the mono-rod cell

(b) dispersion curve of the unit cell, the red dots point out the Dirac point

Figure 3.3: Comparison between the dispersion curve of a unit cell with $U = 24\mu m$ and the corresponding single rod cell

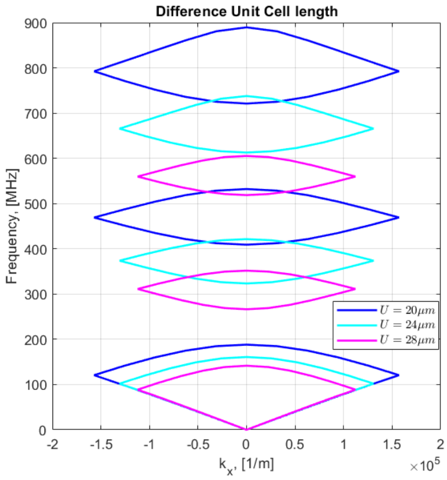

Figure 3.4: Comparison of the dispersion relation of unit cells of different lengths. The cell with a length of $20\mu m$ is shown in blue, while in cyan and magenta, the cells with lengths of $24\mu m$ and $20\mu m$ are shown, respectively.

To establish a topologically protected state following band folding, the introduction of perturbation to the unit cell becomes imperative. Various methods can be employed for this purpose, including modifying material properties or introducing defects. In the specific case under consideration, perturbation is accomplished through a modulation of the unit cell geometry.

A strategic adjustment is made to the spatial arrangement of rods to disrupt the symmetry of the half-cell of origin while preserving unit-cell symmetry. This adjustment results in the definition of two new unit cells, denoted as $A1$ and $A2$, both visually represented in Figure 3.5a. Within the $A1$ unit cell, the distance of the rod from the lateral edge, denoted as $T1$, is reduced compared to the original distance, $T0$. Additionally, the distance between the rod and the symmetric center of the cell is defined as $T_2 = U/2 - R - T_1$. In contrast, the $A2$ cell exhibits the opposite configuration.

Notably, the sum of these two parameters is consistently maintained, equating to $T_1 + T_2 = 2T_0$. This strict preservation is essential to ensure that the band structure generated by these two distinct unit cells remains identical—a condition corroborated by FEM simulation. Figure 3.5 visually reinforces this equivalence, depicting dispersion curves of the $A2$ cell (depicted by black dashed lines) perfectly overlapping with those of the $A1$ cell (depicted in red). This congruous overlap validates the integrity of the band structures generated by both $A1$ and $A2$ unit cells, affirming the success of the geometric perturbation strategy.

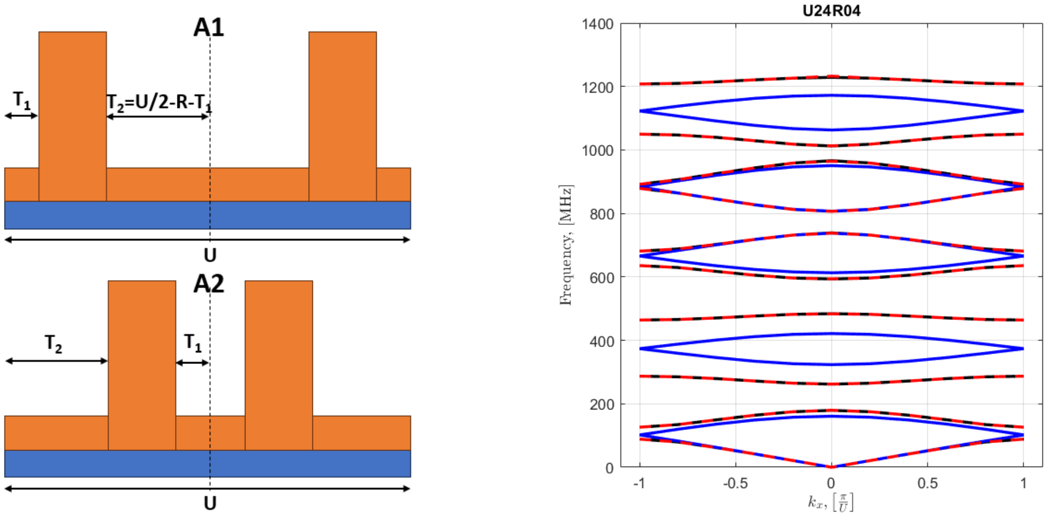

(a) Geometry modulation of the Unit Cell. A1 is on top, and A2 is on the bottom.

(b) Comparison of the dispersion curves of the original unit cell and the new geometries

Figure 3.5:

The introduction of geometric perturbations in the system plays a pivotal role, leading to the emergence of a band gap precisely at the location where topological non-trivial features manifest. This occurrence holds significant importance in the dynamics of the system, serving as a prerequisite, though not an exclusive one, for the generation of a topologically protected edge state.

Essentially, the crucial aspect lies in the necessity of creating a sizable band gap, a task achieved through the influence of geometric perturbations. This band gap formation is particularly critical as it contains the Dirac Point originating in the $A0$ cell. The opening of a sufficiently large band gap not only enhances the system's stability but also facilitates the conditions conducive to establishing a topologically protected edge state. In essence, this intricate interplay between geometric perturbations and band gap formation becomes a key factor in shaping the unique topological characteristics of the system, ultimately leading to the emergence of protected edge states.

The case shown in picture 3.5 is the simulation of a unit cell of lateral length equal to $U = 24\mu m$. The rods are made of Aluminum-Scandium-Nitride, their width is $R = 4\mu m$, and they are $H_{rod} = 400nm$ thick. The bottom layer is made by a $H_m = 80nm$ thick platinum layer, covered by a $H_{tr} = 100nm$ AlScN layer. Therefore, T_0 result equal to $4\mu m$ in the A_0 configuration while, in this case, T_1 have been chosen to be equal to $2\mu m$, thus $T_2 = U/2 - R - T_1 = 6\mu m$. As mentioned above, here we have the confirmation that $T_1 + T_2 = 2T_0 = 8\mu m$.

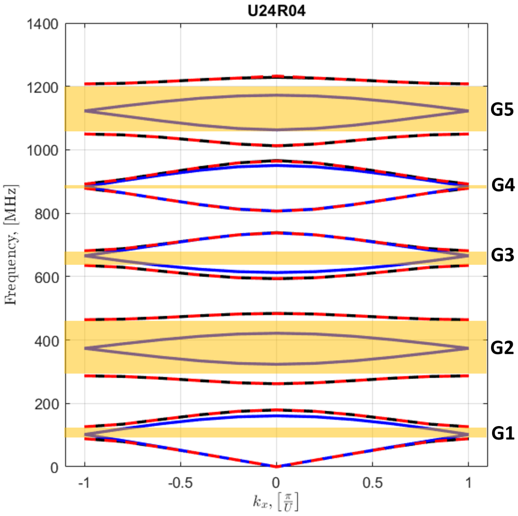

Figure 3.6: Dispersion curve of the unit cell of lateral length $U = 24\mu m$ and rods width $R = 4\mu m$. The yellow bars highlight the band gaps for potential topological protected states.

We can clearly see five band gaps that form around the Dirac points. These frequency gaps are pointed out in Fig.3.6. Two out of the five bandgaps appear more intriguing due to their broader nature, allowing potential edge states to be more isolated and resistant to interference from other states. $G2$ opens around the Dirac Point at $373MHz$, creating a gap of about $126MHz$ and $G5$, is slightly smaller ($158MHz$) but around a higher frequency, $1.12GHz$.

Starting from the same structure, an analysis of possible tuning of different parameters has been made. First of all, a comparison of the dispersion curves obtained as the thickness of the rods is shown in Fig.3.7. As before, the dispersion curves generated from the $A1$ cell, in red, and $A2$, the black dashed line, remain in perfect alignment, and this will not change across all the simulated configurations. It is worth noting that the second band-gap, $G2$, is sustained in both configurations with $R = 6\mu m$ and $R = 2\mu m$. However, a significant reduction in the bandwidth dimension, about 50 MHz, is observed for the latter. This decrease poses a potential challenge for achieving a well-isolated topological edge state. When the rod width is equivalent to $6\mu m$, $G2$ experiences a slight reduction to 161 MHz; however, the Dirac Points are in closer proximity to the higher band. This proximity may similarly present challenges in isolating the edge state effectively.

On the contrary, it is evident that the fifth band gap $G5$ in the original configuration is almost closed in both of the revised configurations. Nevertheless, in both new designs, a novel gap emerges at the fourth band of the $A0$ cell. This underscores the necessity for a thorough investigation into cell design to discern feasible locations for gap opening.

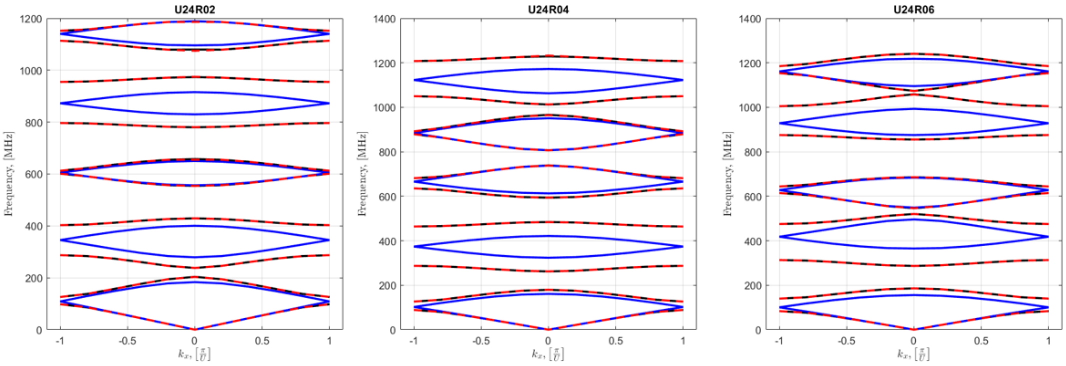

Figure 3.7: Dispersion curve of the same unit cell as the rod width assume values equal to $R = 2\mu m$, $R = 4\mu m$ and $R = 6\mu m$, from left to right respectively

Meanwhile, Fig.3.8 visually demonstrates that variations in the rod thickness exhibit minimal influence on the delineation of the band structure. The observed insensitivity of the band structure to changes in rod thickness suggests a robustness in the system's behavior concerning this specific parameter.

An additional analysis was undertaken to explore potential symmetries within

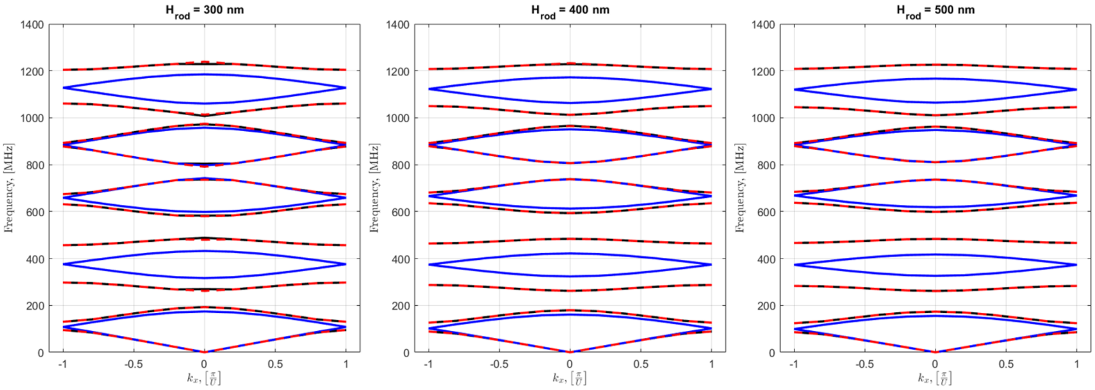

Figure 3.8: Dispersion curve of the same unit cell as the rod thickness change

the configurations of $A1$ and $A2$ cells. This investigation involved varying the parameter T, representing the rod distance from the edge of the cell. Figure 3.9 illustrates the outcomes for $T_{A1} = 1\mu m$ (and $T_{A2} = 7\mu m$) on the left, $T_{A1} = 2\mu m$ ($T_{A2} = 6\mu m$) in the center, and the $A1$ configuration with $T_{A1} = 3\mu m$ ($T_{A2} = 5\mu m$) on the right. The blue lines, consistent with the $A0$ cell, represent $T_{A0} = 4\mu m$.

As T increases and approaches T_{A0}, there is a discernible decrease in the frequencies within the formed bands. This is exemplified by the first two bands when $T = 3\mu m$, which nearly coincide with those of the $A0$ configuration. Notably, when $T = 2\mu m$, precisely half of T_{A0}, the Dirac points align with the midpoint of the generated band gaps.

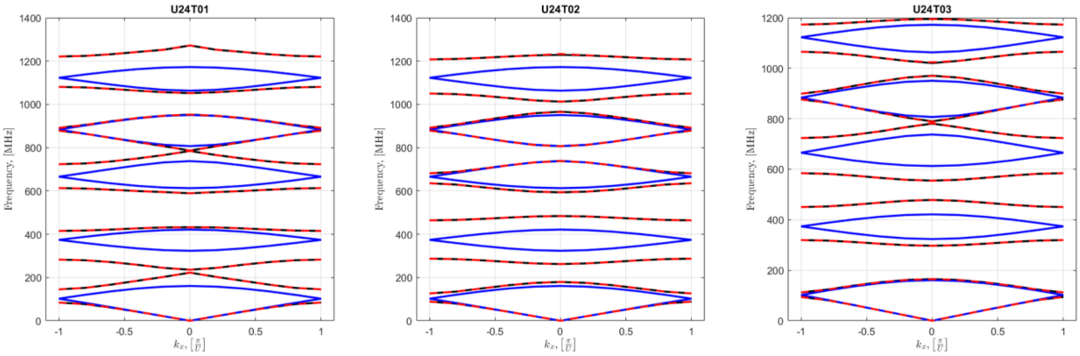

Figure 3.9: Dispersion curve of the same unit cell as the distance T change

In conclusion, an investigation into the variation in the width of the unit cell has been conducted and showed in Fig.3.10. As previously mentioned, the increment in the U parameter results in the narrowing of the frequency distribution within the band, providing a potential avenue for frequency tuning. Furthermore, alterations in the U parameter impact the characteristics of the opened band gaps. While the first gap $G1$ remains consistently open in each design, it is noteworthy that $G2$ contracts for both $U = 20\mu m$ and $U = 28\mu m$, thereby diminishing the likelihood of encountering a topologically protected state.

Simultaneously, with $U = 20\mu m$, a new gap emerges at the fourth band, and for $U = 28\mu m$, one opens at the third band. However, it is crucial to observe that in both instances, the Dirac points are in close proximity to one of the bands of the $A1$ or $A2$ structure. This proximity raises considerations regarding the potential challenges associated with isolating a topologically protected state in these configurations.

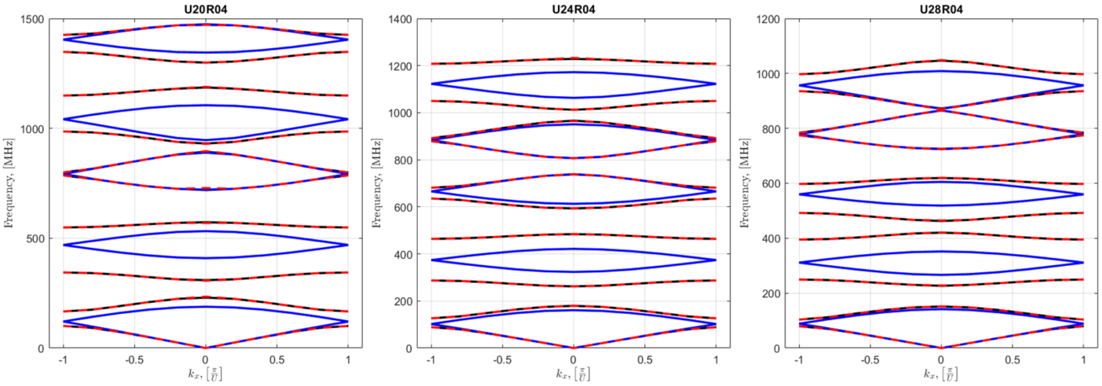

Figure 3.10: Dispersion curve of the unit cell as its lateral dimension U changes

3.2 Zak Phase computation

As mentioned in Chapter 1 and supported by the TKNN theory [7], the primary distinction between a quantum Hall state and a regular insulator is a topological one. This contrast is also applicable to topologically protected surface states in topological insulators. In a 2D bandstructure there exists a mapping from k, the crystal momentum, to the Bloch Hamiltonian, $\mathcal{H}(k)$. The topological classification of gapped band structures involves band structures considering equivalence classes of $\mathcal{H}(k)$ that can be continuously deformed into one another without closing the energy gap[30]. These classes are identified by a topological integer invariant defined as Chern number: $n \in \mathbb{Z}$.

To have a physical perspective of the Chern number, it is necessary to look at that in terms of the Berry phase[31] associated with Bloch wave-functions $|u_m(\boldsymbol{k})\rangle$. Assuming the absence of accidental degeneracies, as $\boldsymbol{k}$ undergoes transport around a closed loop, $|u_m(\boldsymbol{k})\rangle$ accumulates a well-defined Berry phase determined by the line integral of:

$$\mathcal{A}_m = i \langle u_m | \nabla_k | u_m \rangle \tag{3.6}$$

Defining the Berry flux as $\mathcal{F}_m = \nabla \times \mathcal{A}_m$, the Chern number results as the cumulative Berry flux at the Brillouin Zone:

$$n_m = \frac{1}{2\pi} \int d^2\boldsymbol{k} \mathcal{F}_m \tag{3.7}$$

As noted before, n_m is an integer whose quantization is analogous to the Dirac magnetic monopole. The total Chern invariance is then denoted with n and obtained by summing all the n_m for all the occupied bands:

$$n = \sum_{m=1}^{N} n_m \tag{3.8}$$

This total Chern number remains unchanged even in the presence of degeneracies between occupied bands as long as a finite gap persists between occupied bands and empty bands.

3.2.1 Zak phase

When we move to one-dimensional solids, their topological properties are no longer described by the Chern number but by the *Zak phase*. The Zak phase is the Berry's phase acquired by a particle as it moves across the Brillouin Zone.[32].

Being $\psi_k(x)$ a Bloch wave characterized by the quasi-momentum k, the Zak phase φ_{zak} can be conveniently expressed using the cell periodic Bloch function $u_k(x) = e^{-ikx}\psi_k(x)$:

$$\varphi_{zak} = i \int_{-G/2}^{G/2} \langle u_k | \, \partial_k \, | u_k \rangle \, dk \tag{3.9}$$

Here, $G = 2\pi/d$ represents the reciprocal lattice vector, where d is the lattice period and ∂_k is the partial derivative with respect to k. A non-trivial Zak phase underlines the presence of protected edge states.

After the definition of the Zak phase for electronic periodic systems, the concept was extended to acoustic ones[33]. In this case, the geometric phase of the n_{th} isolated band is given by:

$$\theta_n^{zak} = \int_{-\pi/a}^{\pi/a} \left[i \int_{uc} \frac{1}{2\rho\nu^2} d\boldsymbol{r} dx u_{n,k}^*(x, \boldsymbol{r}) \partial_k u_{n,k}(x, \boldsymbol{r}) \right] dk \tag{3.10}$$

where x denotes the axial coordinate, $\boldsymbol{r}$ the position in a cross-sectional plane, uc is the unit cell, ν is the speed of sound, and $u_{n,k}(x, \boldsymbol{r})$ is the periodic in-cell component of the normalized Bloch pressure eigenfunction for a state of wavevector k in the n_{th} band:

$$P_{n,k}(x, \boldsymbol{r}) = u_{n,k}(x, \boldsymbol{r}) e^{ikx} \tag{3.11}$$

The $1/(2\rho\nu^2)$ factor serves as the weight function for the acoustic wave equation. When a quasi-1D system is considered, like when the pressure field in the lateral dimension is uniform, the Zak phase of an isolated band can be derived from the symmetry properties of the band-edge states. When the unit cell exhibits mirror symmetry concerning its central cross-sectional plane, the Zak phase assumes only two possible values: 0 and π. More specifically, if two states at the center and edge of the Brillouin zone within the same band possess the same symmetry, therefore either both even or odd concerning the central plane, then the Zak phase for that band will be equal to 0. On the other hand, if the two states have opposite symmetry, the Zak phase will equal π [34].

A theoretical rationale indicating that the Zak phase of an acoustic system possessing inversion symmetry must be either 0 or π can be provided. Drawing parallels with electronic systems, an analogous Hermitian formulation can be applied to describe an acoustic system. Here, the pressure field corresponds to the electron wave function, while the pressure energy density reflects the probability density of electrons. Consequently, Wannier functions in an acoustic system can be defined, mirroring their electronic counterparts[35]. Assuming a selected origin at $x = 0$, positioned at the middle plane of the system, the center of the Wannier function for the nth band can be linked to the Zak phase of the band through the relation[32]:

$$q_n = \frac{a}{2\pi} \int_{\pi/a}^{\pi/a} \left[i \int_{uc} \frac{1}{2\rho\nu^2} d\overline{r} dx u_{n,k}^*(x, \overline{r}) \partial_k u_{n,k}(x, \overline{r}) \right] dk \tag{3.12}$$

From which it is possible to obtain:

$$q_n = \frac{a}{2\pi}\theta_n^{zak} \tag{3.13}$$

When the acoustic system has periodicity and inversion symmetry, the center of the Wannier function remains invariant under an inversion operation and can be expressed as:

$$q_n = -q_n + ma \tag{3.14}$$

where a is equivalent to the length of the unit cell while m is an integer number. Therefore, as a consequence of Eq.3.14:

$$q_n = 0\, or\, \frac{a}{2} \tag{3.15}$$

Combining Eqs.3.12 and 3.15, it is possible to affirm that, for an acoustic system that has inversion symmetry, its Zak phase can only assume values equal to 0 or to π

3.2.2 Estrapolation of the Zak phase

To deduce the Zak phase of our device, we employed the discretized form of Equation 3.10 [33] [34]:

$$\theta_n^{Zak} = -Im\sum_{i=1}^{N} ln\left[\frac{1}{2\rho\nu^2}\int_{UC} d\boldsymbol{r}dx\, u^*_{n,k_i}(x,\boldsymbol{r})u_{n,k_{i+1}}(x,\boldsymbol{r})\right] \tag{3.16}$$

The eigenfunctions of the unit cell were numerically extracted through a COMSOL simulation of the unit cell. We selected N different points within the Brillouin Zone interval for each distinct band, ranging from $k = -\pi/U$ to $k = \pi/U$. Utilizing Equation 3.16, we obtained the Zak phase in the limit as $\Delta k_i = k_{i+1} - k_i \rightarrow 0$. Subsequently, for each wavevector k value, the eigenpressure was determined for a specific set of points, as illustrated in Fig.3.11:

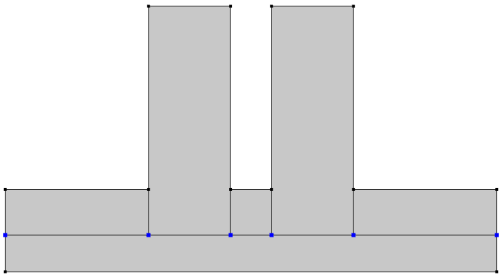

Figure 3.11: Cell point selected to compute the eigenpressure

After obtaining the eigenpressures $u_{n,k_i}(x,\boldsymbol{r})$, a MATLAB code, reported in Appendix A, was implemented to compute the Zak phase for each isolated band.

Numerical results

In this section, we present the results from computing the Zak phase based on the band diagram derived for various unit cell configurations. This computation is of significant importance because when the Zak phase values of the two bands constituting the band gap are inverted between the "symmetry-breaking" configurations, denoted as $A1$ and $A2$, a topologically protected edge state can exist within the gap.

Our initial investigation focused on a scenario involving a symmetric unit cell with a large U of $24\mu m$, featuring AlScN rods with a height (H_{rod}) of $400\,nm$ and a thickness (R) of $4\mu m$. The choice of U and R results in the symmetric unit cell, denoted as A_0, characterized by $T_0 = (U/2 - R)/2 = 4\mu m$. The configurations $A1$ and $A2$ are distinguished by T values of $2\mu m$ and $6\mu m$, respectively, maintaining their sum at $2T_0 = 8\mu m$.

	A1	A2	Gap
θ_1^{Zak}	π	0	G1
θ_2^{Zak}	0	π	
θ_3^{Zak}	0	π	G2
θ_4^{Zak}	0	π	
θ_5^{Zak}	0	π	G3
θ_6^{Zak}	0	π	
θ_7^{Zak}	π	0	G4
θ_8^{Zak}	π	0	
θ_9^{Zak}	0	π	G5
θ_{10}^{Zak}	0	π	

Table 3.1: Zak phase value for each band

Table 3.1 presents the computed Zak phase, denoted as θ_n^{Zak}, for each n_{th} band. The bands are categorized to emphasize the generated gap, as illustrated in Figure 3.6. A detailed examination of the results reveals that, except for the $G1$ gap, none of the formed gaps exhibits an inversion in the geometric phase. Consequently, none of these gaps can support a topologically protected edge state.

This observation is further supported by examining the symmetry of the mode shape with respect to the central cross-section plane of the unit cell. Specifically, when the mode shape at the center and at the edge of the Brillouin Zone for the same band demonstrates identical symmetry, the Zak phase result is $\theta_n^{Zak} = 0$; otherwise, it is equal to π. [36] [37] [34]

Fig.3.12 shows the representation of modes on $k_x = 0$ and $k_x = \pi/U$ for the first two bands of the $A1$ design, on the left and on the right respectively. For the first band, it is possible to notice how the mode in k_0, Fig 3.12(a), is symmetric while the one at the edge of the band is anti-symmetric. Therefore, the geometric phase θ_1^{Zak} is equal to π because the two symmetries are different. Moreover, this result confirms the result reported in 3.1. In the opposite way, the two modes for the second band, shown in 3.12 (c) and (d), are both symmetric. Therefore, the Zak phase for the second band is equal to $\theta_2^{Zak} = 0$

The diagram in Fig.3.12 illustrates the representation for the initial two bands of the $A1$ design of modes at $k_x = 0$ and $k_x = \pi/U$, depicted on the left and right sides, respectively. For the first band, it is observed that the mode at k_0, as shown in Fig.3.12(a), exhibits symmetry, while the mode at the band edge is anti-symmetric. Consequently, the geometric phase θ_1^{Zak} attains a value of π due to the dissimilarity in symmetries. This finding corroborates the results presented in 3.1. Conversely, both modes for the second band, illustrated in Fig.3.12(c) and (d), display symmetry. As a result, the Zak phase for the second band is determined to be $\theta_2^{Zak} = 0$.

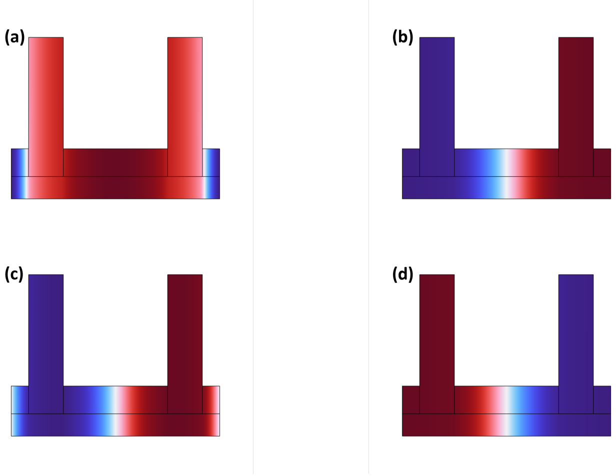

Figure 3.12: Mode shape of the first two $A1$ unit cell configuration bands. Figures (a) and (b) are the first bad modes at $k = 0$ and $k = \pi/U$, respectively. (c) and (d) are the second band modes at $k = 0$ and $k = \pi/U$, respectively

The equivalent analysis is depicted in Fig. 3.13 for the unit cell design $A2$. In contrast, the modes on the first band are both symmetric, while those on the second band possess opposite symmetries. Consequently, in line with our calculations, the Zak phases for the two bands are determined as follows: $\theta_1^{Zak} = 0$ and $\theta_2^{Zak} = \pi$.

Ultimately, the Zak phase for the initial two bands of the $A1$ design undergoes a transition from π to 0, while the opposite trend is observed for the $A2$ configuration. This inversion of symmetry indicates the presence of a topologically protected edge state.

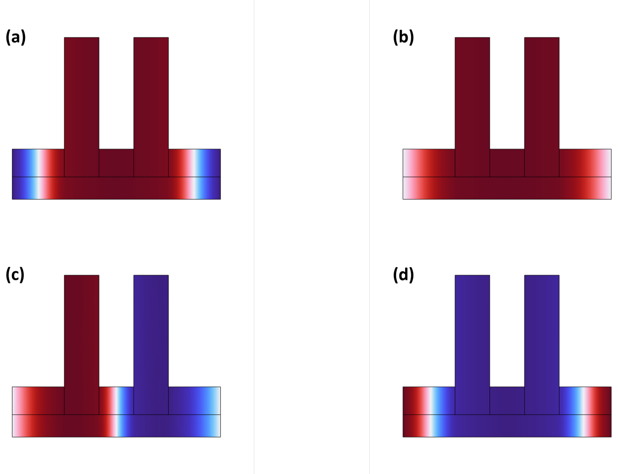

Figure 3.13: Mode shape of the first two $A2$ unit cell configuration bands. Figures (a) and (b) are the first bad modes at $k = 0$ and $k = \pi/U$, respectively. (c) and (d) are the second band modes at $k = 0$ and $k = \pi/U$, respectively

Similarly, an analogous analysis is conducted for the third and fourth bands and it is shown in Fig.3.14 and 3.15. In contrast to the previous observation, both bands for the $A1$ configuration exhibit values of $\theta_3^{Zak} = \theta_4^{Zak} = 0$, while for the $A2$ design, both values are $\theta_3^{Zak} = \theta_4^{Zak} = \pi$. This outcome aligns with the data presented in Table 3.1, indicating the absence of topological inversion and, consequently, the lack of sustained topological protected edge states.

The Zak Phase and mode analysis were conducted for various unit cell configurations. The mode analysis for the additional edge states found in the various studied configurations and the tables containing the computed Zak phases are detailed in Appendix B.

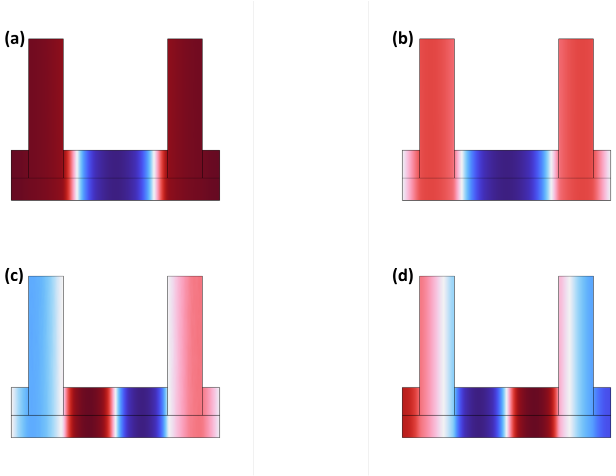

Figure 3.14: Mode shape of the third and fourth $A1$ unit cell configuration bands. Figures (a) and (b) are the third bad modes at $k = 0$ and $k = \pi/U$, respectively. (c) and (d) are the fourth band modes at $k = 0$ and $k = \pi/U$, respectively

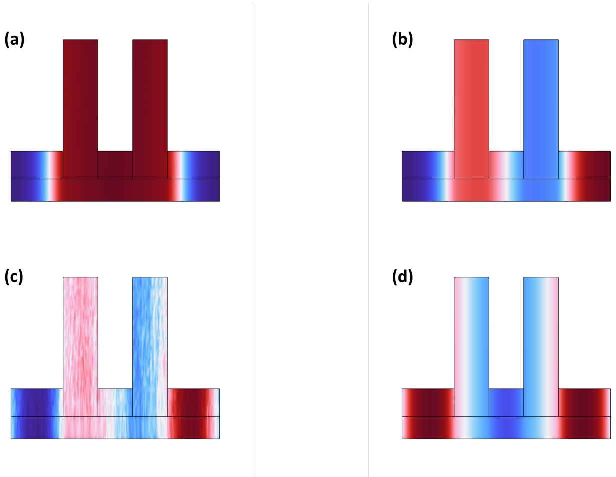

Figure 3.15: Mode shape of the third and fourth $A2$ unit cell configuration bands. Figures (a) and (b) are the third bad modes at $k = 0$ and $k = \pi/U$, respectively. (c) and (d) are the fourth band modes at $k = 0$ and $k = \pi/U$, respectively

Chapter 4

Finite Device Acoustic Simulation

4.1 Finite Device Model

In the course of examining the unit cell, the application of Floquet boundary conditions has allowed the system under investigation to be effectively treated as one comprising an infinite number of unit cells. This strategic approach enables a comprehensive understanding of the system's behavior and properties.

This section delves into the investigation of a finite device through Finite Element Method (FEM) simulations conducted using COMSOL Multiphysics. The primary objective of this analysis is to validate the existence of the topologically protected edge state within a finite device.

Throughout these simulations, emphasis has been placed on exploring two distinct configurations of the device: the $A0A0$ and the $A1A2$. The former constitutes a device composed of N finite $A0$ unit cells, resembling a forest of rods separated by a constant distance—similar in structure to the 2DRR configuration. On the other hand, while sharing similarities, the $A1A2$ configuration can be characterized as a composite phononic system. This designation arises from its composition, featuring two distinct phononic crystals—one comprising $N/2$ $A1$ unit cells and the other $N/2$ $A2$ unit cells. The incorporation of a topological phase inversion at the interface between these two phononic crystals introduces the potential for the formation of the topologically protected edge state.

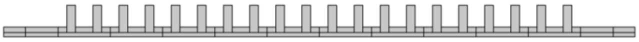

Figure 4.1: Fine $A0A0$ device with $N_{cell} = 10$

Figure 4.2: Fine $A1A2$ device with $N_{cell} = 10$

By exploring these configurations in finite devices, this investigation aims to discern the robustness and practical applicability of the topologically protected edge state in realistic, non-infinite systems.

The device under simulation is made by a bottom platinum plate $80\,nm$ thick on which a $100\,nm$ AlScN layer has been deposited and from which the forest of AlScN rods elevate for $400\,nm$. In order to perform the FEM simulation with the *Pressure Acoustic* package of COMSOL Multiphysics, the Bulk Modulus K and the density of the material ρ are needed. The ones used in this study are reported in Table 4.1

	AlScN	Pt
K	$1.377e^{11}\,Pa$	$2.333e^{11}\,Pa$
ρ	$3700\,kg/m^3$	$21450\,kg/m^3$

Table 4.1: Material parameters

In this preliminary study, the input to the system has been inducted by the application of a Background pressure field of $1\,Pa$ to an extension of the stack of Platinum and Aluminum-Scandium-Nitride, as shown in Fig.4.3.

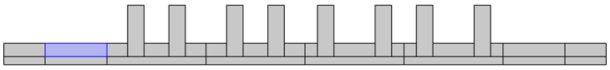

Figure 4.3: Element of a $A1A2$ device formed by $N_{cell} = 4$ cells where it is applied the background pressure field

In COMSOL Multiphysics, the application of a background pressure field is a fundamental aspect of pressure simulations that plays a crucial role in replicating real-world conditions. The background pressure field serves as a reference or baseline pressure within the simulation domain, allowing modeling scenarios where the pressure is not uniformly zero. By incorporating a background pressure field, it is possible to accurately simulate and analyze complex systems, providing a more comprehensive representation of real-world phenomena.

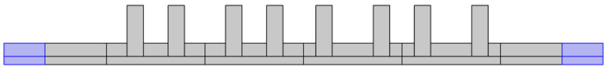

Figure 4.4: PMLs of a $A1A2$ device

Moreover, a *Perfectly Matching Layer* is defined in the device. The PML layer acts as an absorbing boundary condition, effectively dampening outgoing waves and preventing reflections that could distort the accuracy of the simulation results. In acoustic pressure simulations, the PML layer is strategically employed to mitigate artificial reflections at the simulation domain's boundaries, thereby enhancing the precision and reliability of the results. This crucial element ensures that the simulated acoustic field closely mirrors real-world conditions by minimizing boundary artifacts and improving the overall fidelity of the acoustic pressure simulation in COMSOL.

4.2 Transmission Analysis

The main feature that has been studied in our devices is their transmission spectrum. The transmission analysis of a phononic crystal can provide valuable insights into the existence, position, and properties of topologically protected edge states.

To obtain the transfer spectrum of the device, we first define two boundary sources at the beginning (S_1) and at the end (S_2) of our phononic crystal, as shown in Fig.4.5. These two boundaries are necessary to compute the input acoustic power that will be the reference, P_{ref}, and output power, P_{out}. The first is computed by performing the integral of the input pressure p_0 over the density ρ and the speed of sound in the material c_m:

$$P_{in} = 2 \int_{S_1} \frac{p_0^2}{2\rho c} \tag{4.1}$$

while the output power can be obtained by just integrating the x component of the acoustic intensity on the surface S_2:

$$P_{out} = \int_{S_2} I_x \tag{4.2}$$

The final transmission is then computed as the ratio between the output power and the reference one: $T = P_{out}/P_{ref}$.

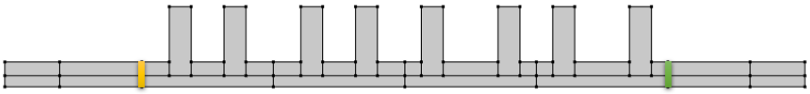

Figure 4.5: S_1 and S_2 integration surfaces, in yellow and blue respectively

First of all, a comparison between the dispersion curves was obtained in Chapter.3 and the transfer plot obtained is made to validate the obtained results' coherence. The comparison is illustrated in Fig.4.6, wherein a finite device comprising a total of 8 unit cells of width equal to $U = 24\mu m$ is examined. The lower metal component consists of an $80\,nm$ thick Pt layer, while the trench layer is composed of a $H_{th} = 100\,nm$ AlScN layer, and the rods exhibit a thickness denoted as $H_{rod} = 400\,nm$. In both graphs, the blue lines represent the $A0A0$ configuration, denoting the fully symmetric configuration with a unit cell characteristic equal to $T = (U/2 - R)/2 = 4\mu m$. Conversely, the red lines pertain to the $A1A2$ configuration characterized by $T_{A1} = 6\mu m$ and $T_{A2} = 2\mu m$. A discernible alignment is observed between the dispersion curve and the transmission spectrum. Notably, there exists a transmission within the finite device that corresponds to the bands depicted in the initial graph. Nevertheless, it is evident that an exact correspondence between the frequency of the band and the passbands in the transmission spectrum is lacking. This discrepancy is attributed to a detectable downward shift in frequencies within the finite device, and this shift becomes more pronounced with an escalation in frequency.

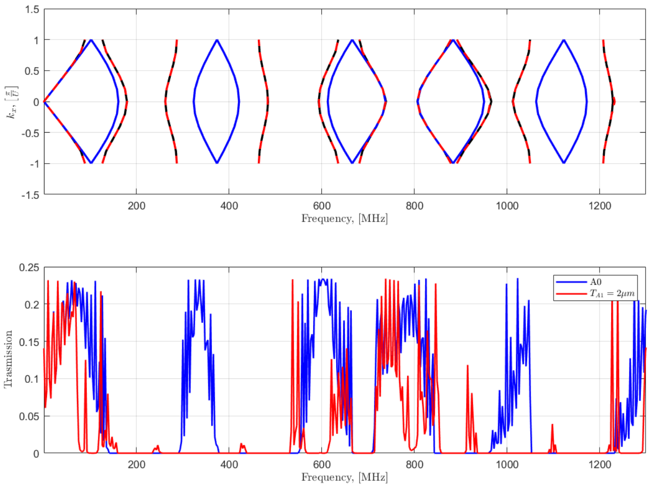

Figure 4.6: Dispersion curve, on top, and Transmission of a device made by 8 unit cells

Figure 4.7 depicts the outcomes of the device constructed with $N = 10$ unit cells, maintaining a consistent configuration. Similar to the observations in the preceding analysis, a noticeable coherence with the bands derived from the unit-cell analysis is evident here. The presence of a frequency shift, observed with respect to the band diagram, is discernibly comparable to the shift illustrated in Figure 4.6 for the 8 unit cell device. This consistency in the frequency shift prompts considerations that the observed alteration in frequency may be attributed to the additional lateral component employed to impart input pressure to the system.

Both of these illustrations further validate the emergence of band-gaps surrounding the Dirac points upon the disruption of unit-cell symmetry. In Figure 4.8, the depiction illustrates the appearance of these gaps both in devices formed exclusively by symmetry-breaking unit cells of the same type (specifically, the $A1A1$, in orange, and the $A2A2$, in yellow, configurations), and when half of the device comprises unit-cells of one type while the other half comprises the specular unit-cell type. Remarkably, these arrangements yield identical outcomes when the two sides are inverted, exemplified in both the $A1A2$ and $A2A1$ configurations in magenta and cyan, respectively.

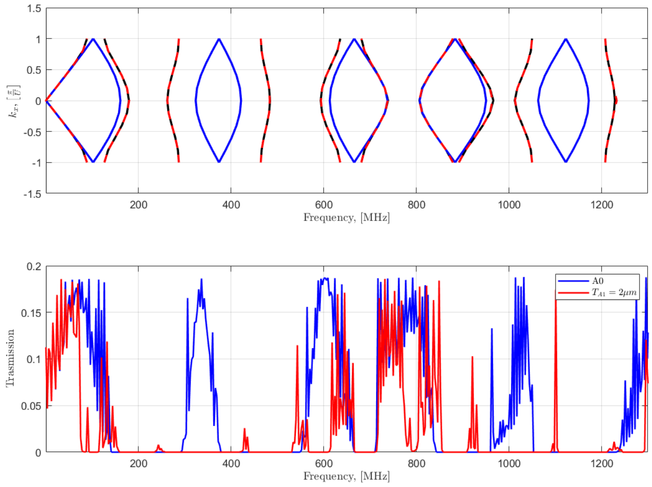

Figure 4.7: Dispersion curve, on top, and Transmission of a device made by 10 unit cells

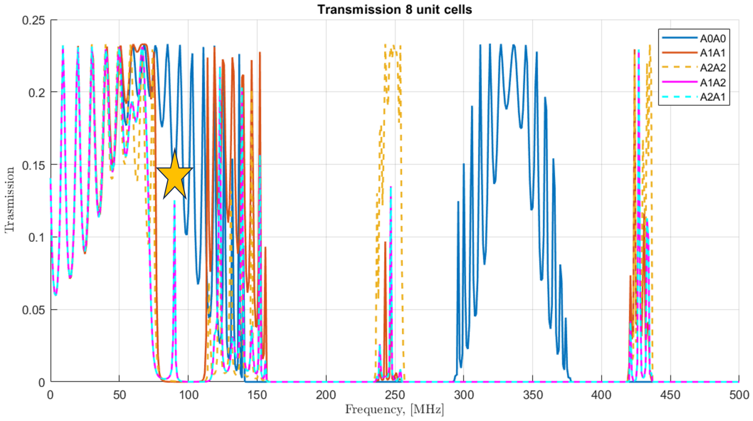

Figure 4.8: Transmission graph of the five combinations of unit cells: $A0A0$, $A1A1$, $A2A2$, $A1A2$, and $A2A1$. The yellow star highlights the topologically protected edge state.

These visual representations already confirm the presence of a topologically protected edge state at approximately 90 MHz. Notably, this state exclusively manifests in the $A1A2$ or $A2A1$ configurations, affirming that the topological phase inversion is specifically inherent in these configurations.

Figure 4.9 illustrates the transmission spectrum of a device configured as $A1A2$ within the frequency range of 0 to 160 MHz specifically focusing on the edge state.

An anticipated trend is observed wherein the transmission diminishes with an increasing number of unit cells. Notably, the edge state mirrors this attenuation, remaining perceptible in a device composed of 8 unit cells but exhibiting a gradual decline in visibility with a continued rise in the number of unit cells until its complete disappearance in a device comprised of 16 unit cells.

Conversely, in instances involving a lower quantity of unit cells, the edge state manifests a more pronounced peak. However, the associated band gap is less well-defined, resulting in a state that is not effectively isolated.

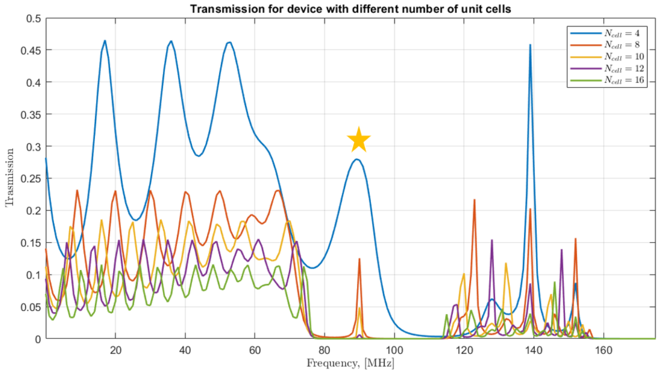

Figure 4.9: Focus on the topologically protected edge state for devices made by a different number of unit cells

Shifting the focus to the behavior of the edge state with variations in the parameter T, it becomes apparent that the intensity of this state is influenced by the symmetry of the unit cell. Specifically, as the separation between the two rods converges toward that of the $A0$ configuration ($T_0 = 4\mu m$), the transmission associated with the edge state escalates. However, approaching the $A0$ configuration results in a less distinct band gap, consequently diminishing the clarity of the edge state.

For $T = 2\mu m$, while the peak exhibits a value comparable to the preceding scenario, the open gap is well-defined, thereby ensuring the robust delineation of the topological state.

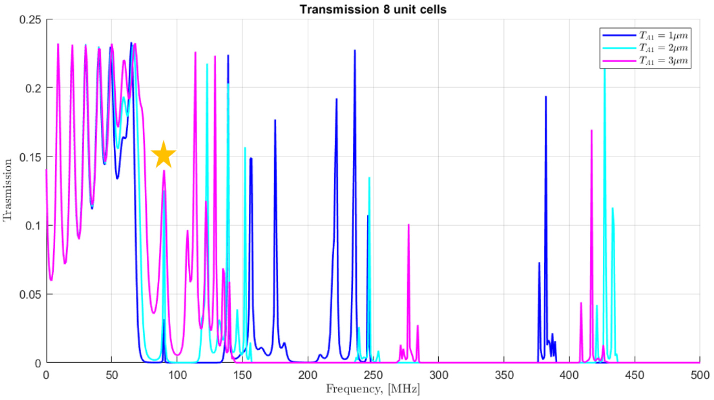

Figure 4.10: Transmission graph of the $A1A2$ device made with a different number of unit cells. At 90 MHz the presence, or not, of the topologically protected edge state

The topologically protected mode at $90, MHz$ is depicted in Figure 4.11a. As anticipated, the transmission is observed throughout the entire device, with the field concentration evident at the interface between the two sides of the $A1A2$ configuration. Conversely, in Figure 4.11b, a complete absence of transmission is observed, indicating the absence of the edge state.

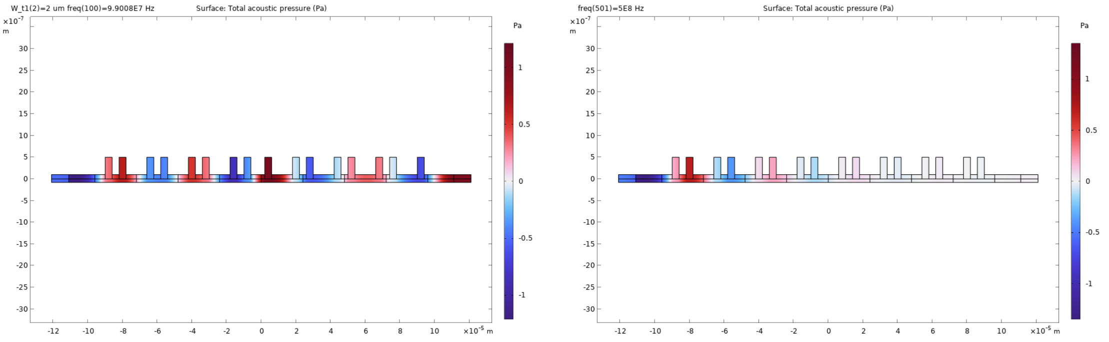

(a) Presence of the topological protected state at frequency $f = 90MHz$ in the $A1A2$ device

(b) Absence of the topological protected state at frequency $f = 90MHz$ in the $A1A1$ device

Figure 4.11: Presence and absence of the topologically protected state in $A1A2$ configuration and $A1A1$, respectively

Conducting an analysis of the device while varying the width of the unit cells U, it is evident that for smaller U values, such as $U = 20\mu m$ in Figure 4.12, the peak associated with the topological state diminishes considerably. However, as U is increased, the edge state at 90 MHz becomes more pronounced, and notably, a second edge state emerges around 500 MHz, as depicted in figure 4.13 for $U = 28\mu m$.

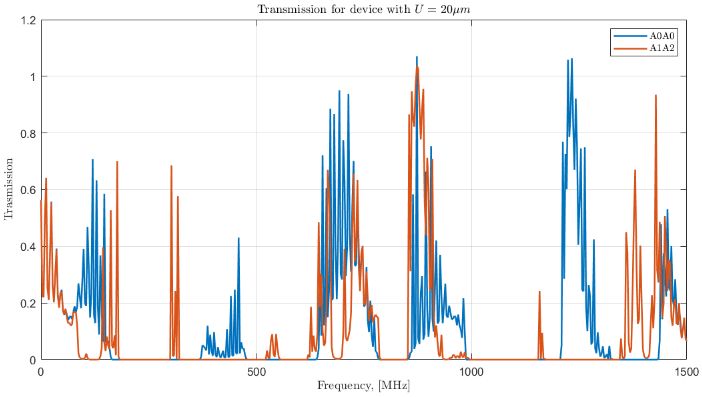

Figure 4.12: Transmission graph of the $A1A2$ device made with unit cells of lateral length $U = 20\mu m$

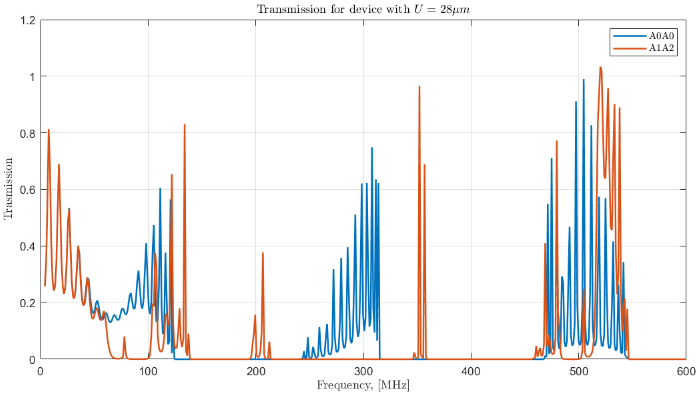

Figure 4.13: Transmission graph of the $A1A2$ device made with unit cells of lateral length $U = 28\mu m$

Also, when the thickness of the rod is increased to $R = 6\mu m$, another topological state is confirmed around 696 MHz other than the one that is present in the first bandgap that is not present when the R decreases.

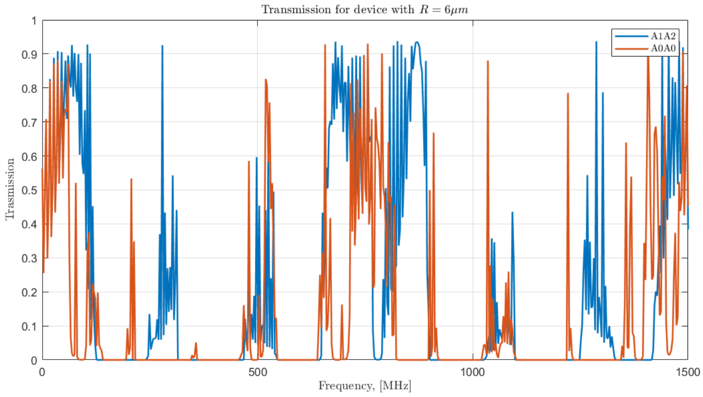

Figure 4.14: Transmission graph of the $A1A2$ device made with rod of thickness $R = 6\mu m$

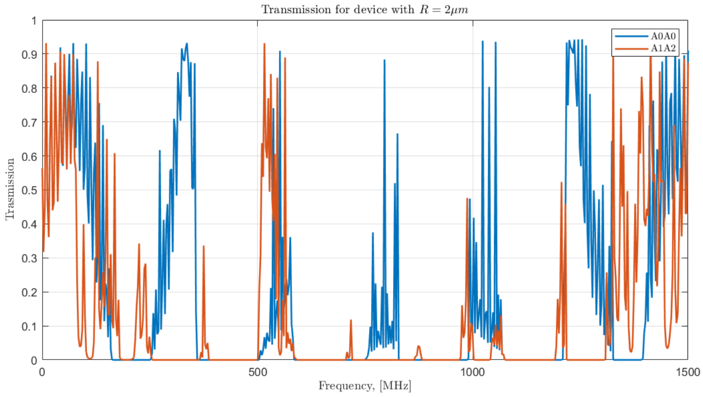

Figure 4.15: Transmission graph of the $A1A2$ device made with rod of thickness $R = 2\mu m$

Ultimately, the transmission spectrum of the device is scrutinized with rods of varying heights. Notably, the persistence of the topologically protected edge state within the first band gap is sustained, both when the rod height is reduced to $H_{rod} = 300, nm$ (as depicted in Fig.4.16) and when increased to $H_{rod} = 500nm$ (as illustrated in Fig.4.17). In the former case, another topologically protected edge state is also discerned at $591, MHz$; however, its intensity is notably diminutive, suggesting potential absence in practical device implementations.

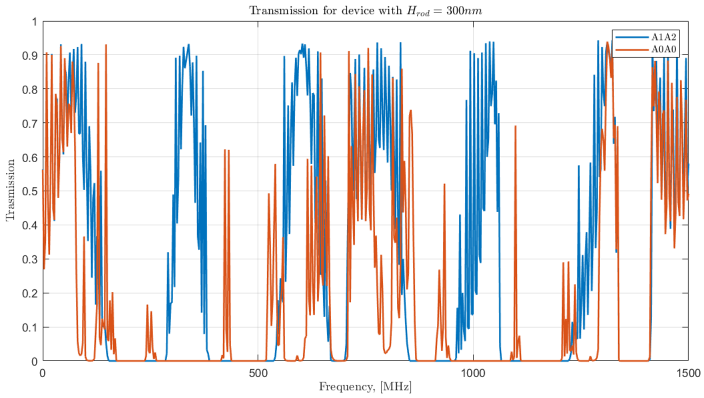

Figure 4.16: Transmission graph of the $A1A2$ device made with rod of height $H_{rod} = 300\,nm$

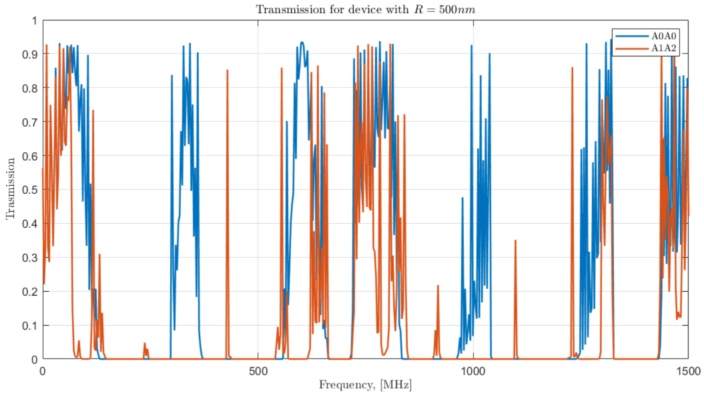

Figure 4.17: Transmission graph of the $A1A2$ device made with rod of height $H_{rod} = 500\,nm$

Chapter 5

Conclusions

The growing interest in topologically non-trivial systems, coupled with advancements in Micro-Electro-Mechanical Systems (MEMS) that enable the development of acoustic metamaterials with tailored acoustic properties, has stimulated this work: the creation of a micro-electro-mechanical device designed to sustain a topologically protected edge state.

The investigation conducted involved an in-depth study of the unit cell, leading to the development of a metamaterial exhibiting non-trivial topological properties. This rigorous examination provided critical insights into the influence of design parameters on the band structure. The identification of the topologically protected edge state was achieved through the use of topologically invariant measures, such as the Zak phase. Subsequent finite device analysis expanded this exploration, uncovering the emergence and sensitivity of topologically protected edge states across diverse device configurations.

Future developments in this research will entail a detailed examination of unit cell design using the transmission matrix approach, aiming to obtain a robust analytical characterization of the acoustic metamaterial. Additionally, experimental results obtained from fabricated devices will be analyzed to comprehend their behavior in real-case scenarios.

This comprehensive study has contributed significantly to our understanding of topological states in Piezo-Electric MEMS devices, and it has laid the foundation for potential applications in the RF spectrum. The study highlights how topological states respond to different design parameters and how they can be practically applied in real-world situations. This research opens avenues for further advancements in integrating MEMS technology with topologically acoustic devices, which has the potential to bring innovations in RF communication, filtering, and signal processing.

Appendix A

MATLAB CODE for the Zak Phase computation

```matlab
%Preconditioning
clear all
close all
clc

filename = uigetfile('*.xlsx');
opts = detectImportOptions(filename);
preview(filename,opts);

%% Zak Phase Calculation
for k = 1:2
    opts.Sheet=k;
    T1 = readtable(filename,opts);
    SzT = size(T1);
    Nvar = SzT(2);
    Tkx = 2; %starting at Tkx column, it's the value of kx

    kx = table2array(T1(:,Tkx));
    BZ=length(kx)-1; % how many kx-points in BZ (the last one is the same as the first, so need to remove)
    Ns = 10; % total solution number
    Wu = 24e-6; % unitcell length
    L= (Nvar - Tkx)/Ns; % how many x-points in the unit cell + the other parameters (e.g. A2, A0, kx, etc)
    P1=Tkx+1; % in the table, which column is the first solution for the fitrst x point

    Vfield = T1(:,P1:Nvar);
```

```
        Vcell = table2cell(Vfield);
        Vcomp0 = str2double(Vcell);
        for n= 1:Ns % sweep solution number
            Vcomp = Vcomp0(:,1+(n-1)*L:L+(n-1)*L);
            for q = 1:L % Unit-cell (Position)
                for j = 1:BZ-1 % BZ except for last point (Bloch & kx)
                    Prod(j,q) = dot(conj(Vcomp(j,q)), Vcomp(j+1,q));
                end
                Prod(BZ,q) = dot(conj(Vcomp(BZ,q)), Vcomp(1,q)*exp(-i*2*pi/Wu*(q-1)*Wu/(L-1)));
            end
            for j=1:BZ
                SumIN(j) = sum(Prod(j,:));
                LOG(j)=log(SumIN(j));
                PHI(j)=-imag(LOG(j)); % Berry phase
            end
            Zak(n,k) = sum((PHI));
            Zak_mod = mod(Zak, (2*pi))

            Zak_Table = array2table(Zak_mod);
            Zak_sum(n,k) = sum(Zak(:,k));
            figure;
            P = [220 220 235 225];
            PHI(BZ+1)=PHI(1);
            set(gcf, 'Position', P);
            scatter(kx*Wu,PHI);
            ylim([-3.2,3.2]);
            hold on
            grid on
        end
    end
```

Appendix B

Result of Zak Phase computation

Changing distance from the edge T

$T_1 = 1$	θ_1^{Zak}	θ_2^{Zak}	θ_3^{Zak}	θ_4^{Zak}	θ_5^{Zak}	θ_6^{Zak}	θ_7^{Zak}	θ_8^{Zak}	θ_9^{Zak}	θ_{10}^{Zak}
A1	π	0	0	0	0	$0i$	π	π	0	0
A2	0	π	π	π	π	π	0	0	π	π

Table B.1: Zak phase value for a unit cell with parameter: $U = 24\mu m$, $R = 4\mu m$, $H_{rod} = 400nm$, $T_{A1} = 1\mu m$ and $T_{A2} = 7\mu m$

$T_1 = 3$	θ_1^{Zak}	θ_2^{Zak}	θ_3^{Zak}	θ_4^{Zak}	θ_5^{Zak}	θ_6^{Zak}	θ_7^{Zak}	θ_8^{Zak}	θ_9^{Zak}	θ_{10}^{Zak}
A1	π	0	0	0	0	$0i$	π	π	0	0
A2	0	π	π	π	π	π	0	0	π	π

Table B.2: Zak phase value for a unit cell with parameter: $U = 24\mu m$, $R = 4\mu m$, $H_{rod} = 400nm$, $T_{A1} = 3\mu m$ and $T_{A2} = 5\mu m$

Changing unit cell width U

$U = 20$	θ_1^{Zak}	θ_2^{Zak}	θ_3^{Zak}	θ_4^{Zak}	θ_5^{Zak}	θ_6^{Zak}	θ_7^{Zak}	θ_8^{Zak}	θ_9^{Zak}	θ_{10}^{Zak}
A1	π	0	0	0	π	π	0	0	π	π
A2	0	π	π	π	0	0	π	π	0	0

Table B.3: Zak phase value for a unit cell with parameter: $U = 20\mu m$, $R = 4\mu m$, $H_{rod} = 400nm$, $T_{A1} = 1.5\mu m$ and $T_{A2} = 4.5\mu m$

$U = 28$	θ_1^{Zak}	θ_2^{Zak}	θ_3^{Zak}	θ_4^{Zak}	θ_5^{Zak}	θ_6^{Zak}	θ_7^{Zak}	θ_8^{Zak}	θ_9^{Zak}	θ_{10}^{Zak}
A1	π	0	0	0	π	0	0	0	π	π
A2	0	π	π	π	0	π	π	π	0	0

Table B.4: Zak phase value for a unit cell with parameter: $U = 28\mu m$, $R = 4\mu m$, $H_{rod} = 400nm$, $T_{A1} = 2.5\mu m$ and $T_{A2} = 7.5\mu m$

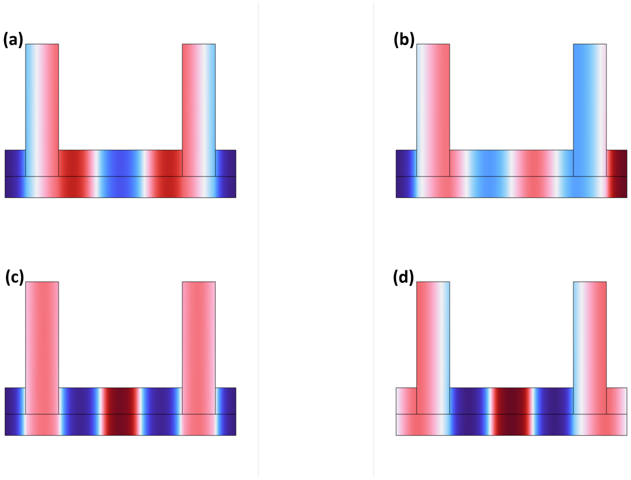

Figure B.1: Mode shape of the fifth and sixth bands of the $A1$ unit cell configuration with $U = 28\mu m$

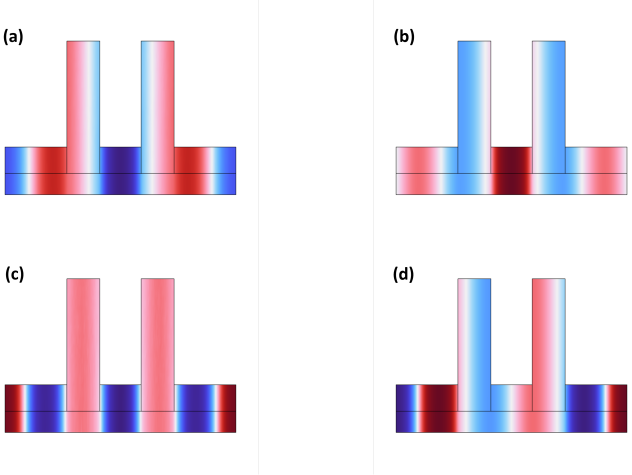

Figure B.2: Mode shape of the fifth and sixth bands of the $A2$ unit cell configuration with $U = 28\mu m$

Changing rod height H_{rod}

$H_r = 300nm$	θ_1^{Zak}	θ_2^{Zak}	θ_3^{Zak}	θ_4^{Zak}	θ_5^{Zak}	θ_6^{Zak}	θ_7^{Zak}	θ_8^{Zak}	θ_9^{Zak}	θ_{10}^{Zak}
A1	π	0	0	0	π	0	π	π	π	π
A2	0	π	π	π	0	π	0	0	0	0

Table B.5: Zak phase value for a unit cell with parameter: $U = 24\mu m$, $R = 4\mu m$, $H_{rod} = 300nm$, $T_{A1} = 2\mu m$ and $T_{A2} = 6\mu m$

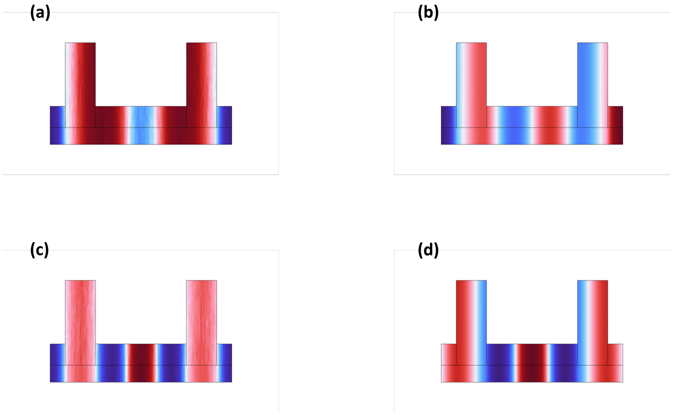

Figure B.3: Mode shape of the fifth and sixth bands of the $A1$ unit cell configuration with $U = 28\mu m$

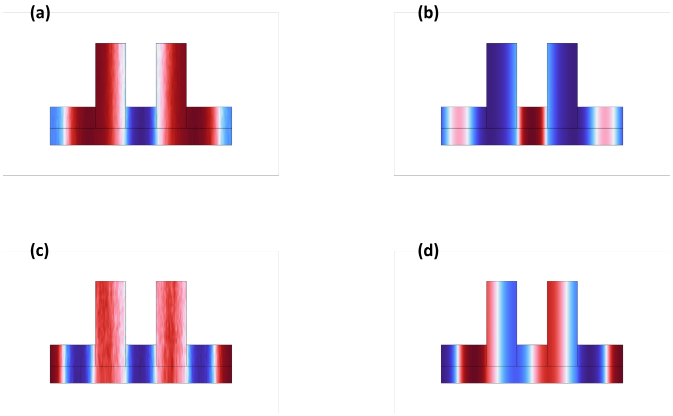

Figure B.4: Mode shape of the fifth and sixth bands of the $A2$ unit cell configuration with $U = 28\mu m$

$H_r = 300nm$	θ_1^{Zak}	θ_2^{Zak}	θ_3^{Zak}	θ_4^{Zak}	θ_5^{Zak}	θ_6^{Zak}	θ_7^{Zak}	θ_8^{Zak}	θ_9^{Zak}	θ_{10}^{Zak}
A1	π	0	0	0	π	π	π	π	π	π
A2	0	π	π	π	0	0	0	0	0	0

Table B.6: Zak phase value for a unit cell with parameter: $U = 24\mu m$, $R = 4\mu m$, $H_{rod} = 500nm$, $T_{A1} = 2\mu m$ and $T_{A2} = 6\mu m$

Changing rod width R

$R = 6$	θ_1^{Zak}	θ_2^{Zak}	θ_3^{Zak}	θ_4^{Zak}	θ_5^{Zak}	θ_6^{Zak}	θ_7^{Zak}	θ_8^{Zak}	θ_9^{Zak}	θ_{10}^{Zak}
A1	π	0	π	π	π	π	π	0	π	π
A2	0	π	π	π	π	π	0	π	π	π

Table B.7: Zak phase value for a unit cell with parameter: $U = 24\mu m$, $R = 6\mu m$, $H_{rod} = 400nm$, $T_{A1} = 1.5\mu m$ and $T_{A2} = 4.5\mu m$

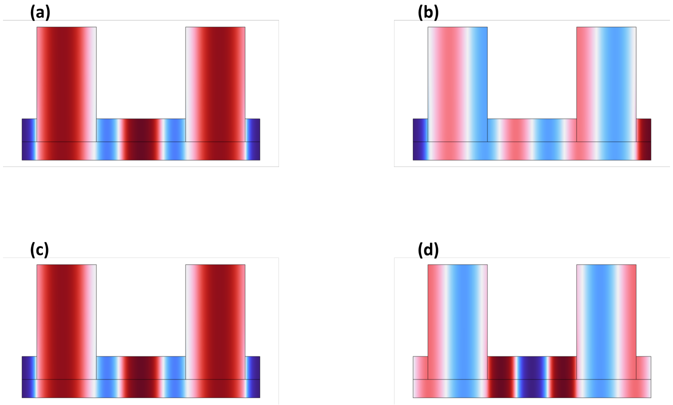

Figure B.5: Mode shape of the seventh and eighth bands of the $A1$ unit cell configuration with $U = 28\mu m$

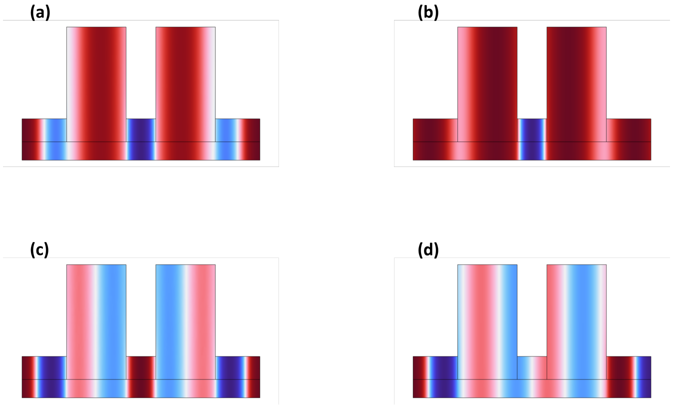

Figure B.6: Mode shape of the seventh and eighth bands of the $A2$ unit cell configuration with $U = 28\mu m$

$R = 2$	θ_1^{Zak}	θ_2^{Zak}	θ_3^{Zak}	θ_4^{Zak}	θ_5^{Zak}	θ_6^{Zak}	θ_7^{Zak}	θ_8^{Zak}	θ_9^{Zak}	θ_{10}^{Zak}
A1	π	0	π	π	π	π	π	π	π	π
A2	0	π	π	π	π	π	π	π	π	π

Table B.8: Zak phase value for a unit cell with parameter: $U = 24\mu m$, $R = 2\mu m$, $H_{rod} = 400nm$, $T_{A1} = 2.5\mu m$ and $T_{A2} = 7.5\mu m$

Bibliography

[1] M. M. Sigalas and E. N. Economou. «Elastic and acoustic wave band structure». In: *Journal of Sound Vibration* 158.2 (Oct. 1992), pp. 377–382. DOI: `10.1016/0022-460X(92)90059-7` (cit. on p. 1).

[2] M. S. Kushwaha, P. Halevi, L. Dobrzynski, and B. Djafari-Rouhani. «Acoustic band structure of periodic elastic composites». In: *Phys. Rev. Lett.* 71 (13 Sept. 1993), pp. 2022–2025. DOI: `10.1103/PhysRevLett.71.2022`. URL: `https://link.aps.org/doi/10.1103/PhysRevLett.71.2022` (cit. on p. 1).

[3] N.W. Ashcroft and N.D. Mermin. *Solid State Physics.* HRW international editions. Holt, Rinehart and Winston, 1976. ISBN: 9780030839931 (cit. on p. 5).

[4] V. Romero-García J.-P. Groby N. Jiménez. *Acoustic Waves in Periodic Structures, Metamaterials, and Porous Media.* Springer, 2021 (cit. on p. 7).

[5] K. v. Klitzing, G. Dorda, and M. Pepper. «New Method for High-Accuracy Determination of the Fine-Structure Constant Based on Quantized Hall Resistance». In: *Phys. Rev. Lett.* 45 (6 Aug. 1980), pp. 494–497. DOI: `10.1103/PhysRevLett.45.494`. URL: `https://link.aps.org/doi/10.1103/PhysRevLett.45.494` (cit. on p. 8).

[6] R. B. Laughlin. «Quantized Hall conductivity in two dimensions». In: 23.10 (May 1981), pp. 5632–5633. DOI: `10.1103/PhysRevB.23.5632` (cit. on p. 8).

[7] D. J. Thouless, M. Kohmoto, M. P. Nightingale, and M. den Nijs. «Quantized Hall Conductance in a Two-Dimensional Periodic Potential». In: *Phys. Rev. Lett.* 49 (6 Aug. 1982), pp. 405–408. DOI: `10.1103/PhysRevLett.49.405`. URL: `https://link.aps.org/doi/10.1103/PhysRevLett.49.405` (cit. on pp. 8, 32).

[8] C. L. Kane and E. J. Mele. «Quantum Spin Hall Effect in Graphene». In: *Phys. Rev. Lett.* 95 (22 Nov. 2005), p. 226801. DOI: `10.1103/PhysRevLett.95.226801`. URL: `https://link.aps.org/doi/10.1103/PhysRevLett.95.226801` (cit. on p. 8).

[9] Wang Yao, Di Xiao, and Qian Niu. «Valley-dependent optoelectronics from inversion symmetry breaking». In: *Phys. Rev. B* 77 (23 June 2008), p. 235406. DOI: `10.1103/PhysRevB.77.235406`. URL: `https://link.aps.org/doi/10.1103/PhysRevB.77.235406` (cit. on p. 8).

[10] Xiangdong Zhang. «Observing Zitterbewegung for Photons near the Dirac Point of a Two-Dimensional Photonic Crystal». In: *Phys. Rev. Lett.* 100 (11 Mar. 2008), p. 113903. DOI: `10.1103/PhysRevLett.100.113903`. URL: `https://link.aps.org/doi/10.1103/PhysRevLett.100.113903` (cit. on p. 9).

[11] Xiangdong Zhang and Zhengyou Liu. «Extremal Transmission and Beating Effect of Acoustic Waves in Two-Dimensional Sonic Crystals». In: *Phys. Rev. Lett.* 101 (26 Dec. 2008), p. 264303. DOI: `10.1103/PhysRevLett.101.264303`. URL: `https://link.aps.org/doi/10.1103/PhysRevLett.101.264303` (cit. on p. 9).

[12] Jiuyang Lu, Chunyin Qiu, Manzhu Ke, and Zhengyou Liu. «Valley Vortex States in Sonic Crystals». In: *Phys. Rev. Lett.* 116 (9 Feb. 2016), p. 093901. DOI: `10.1103/PhysRevLett.116.093901`. URL: `https://link.aps.org/doi/10.1103/PhysRevLett.116.093901` (cit. on p. 9).

[13] Sai Sanjit Ganti, Ting-Wei Liu, and Fabio Semperlotti. «Topological edge states in phononic plates with embedded acoustic black holes». In: *Journal of Sound and Vibration* 466 (2020), p. 115060. ISSN: 0022-460X. DOI: `https://doi.org/10.1016/j.jsv.2019.115060`. URL: `https://www.sciencedirect.com/science/article/pii/S0022460X19306236` (cit. on pp. 9, 10).

[14] Yuanchen Deng, Hao Ge, Yuan Tian, Minghui Lu, and Yun Jing. «Observation of zone folding induced acoustic topological insulators and the role of spin-mixing defects». In: *Phys. Rev. B* 96 (18 Nov. 2017), p. 184305. DOI: `10.1103/PhysRevB.96.184305`. URL: `https://link.aps.org/doi/10.1103/PhysRevB.96.184305` (cit. on p. 10).

[15] Hongfei Zhu, Ting-Wei Liu, and Fabio Semperlotti. «Design and experimental observation of valley-Hall edge states in diatomic-graphene-like elastic waveguides». In: *Phys. Rev. B* 97 (17 May 2018), p. 174301. DOI: `10.1103/PhysRevB.97.174301`. URL: `https://link.aps.org/doi/10.1103/PhysRevB.97.174301` (cit. on p. 10).

[16] Ting-Wei Liu and Fabio Semperlotti. «Tunable Acoustic Valley–Hall Edge States in Reconfigurable Phononic Elastic Waveguides». In: *Phys. Rev. Appl.* 9 (1 Jan. 2018), p. 014001. DOI: `10.1103/PhysRevApplied.9.014001`. URL: `https://link.aps.org/doi/10.1103/PhysRevApplied.9.014001` (cit. on p. 10).

[17] Wang Yao, Shengyuan A. Yang, and Qian Niu. «Edge States in Graphene: From Gapped Flat-Band to Gapless Chiral Modes». In: *Phys. Rev. Lett.* 102 (9 Mar. 2009), p. 096801. DOI: `10.1103/PhysRevLett.102.096801`. URL: `https://link.aps.org/doi/10.1103/PhysRevLett.102.096801` (cit. on p. 11).

[18] Harmeet Bhugra and Gianluca Piazza. *Piezoelectric MEMS resonators*. Springer, 2017 (cit. on pp. 14, 16, 19).

[19] Oliver Brand, Isabelle Dufour, Stephen Heinrich, and Fabien Josse. *Resonant MEMS: Fundamentals, Implementation, and Application*. Jan. 2015 (cit. on p. 18).

[20] B. Bahreyni. «Fabrication and Design of Resonant Microdevices». In: *Fabrication and Design of Resonant Microdevices* (Jan. 2009) (cit. on p. 18).

[21] Cristian Cassella, Yu Hui, Zhenyun Qian, Gwendolyn Hummel, and Matteo Rinaldi. «Aluminum Nitride Cross-Sectional Lamé Mode Resonators». In: *Journal of Microelectromechanical Systems* 25.2 (2016), pp. 275–285. DOI: `10.1109/JMEMS.2015.2512379` (cit. on p. 19).

[22] Ming-Hui Lu, Liang Feng, and Yan-Feng Chen. «Phononic crystals and acoustic metamaterials». In: *Materials Today* 12.12 (2009), pp. 34–42. ISSN: 1369-7021. DOI: `https://doi.org/10.1016/S1369-7021(09)70315-3`. URL: `https://www.sciencedirect.com/science/article/pii/S1369702109703153` (cit. on p. 20).

[23] Tzung-Chen Wu, Tsung-Tsong Wu, and Jin-Chen Hsu. «Waveguiding and frequency selection of Lamb waves in a plate with a periodic stubbed surface». In: *Phys. Rev. B* 79 (10 Mar. 2009), p. 104306. DOI: `10.1103/PhysRevB.79.104306`. URL: `https://link.aps.org/doi/10.1103/PhysRevB.79.104306` (cit. on p. 20).

[24] X. Rottenberg, R. Jansen, P. Verheyen, R. Van Hoof, A. Verbist, and H.A.C. Tilmans. «Engineering of acoustic metamaterials with application to MEMS BAW resonators». In: *2011 16th International Solid-State Sensors, Actuators and Microsystems Conference*. 2011, pp. 930–933. DOI: `10.1109/TRANSDUCERS.2011.5969702` (cit. on p. 20).

[25] Xuanyi Zhao, Luca Colombo, and Cristian Cassella. «Aluminum nitride two-dimensional-resonant-rods». In: *Applied Physics Letters* 116.14 (Apr. 2020). ISSN: 1077-3118. DOI: `10.1063/5.0005203`. URL: `http://dx.doi.org/10.1063/5.0005203` (cit. on pp. 20, 22).

[26] Xuanyi Zhao, Onurcan Kaya, Michele Pirro, Pietro Simeoni, Jeronimo Segovia-Fernandez, and Cristian Cassella. «Extending the Linearity of AlScN Contour-Mode Resonators Through Acoustic Metamaterials-Based Reflectors». In: *IEEE Transactions on Ultrasonics, Ferroelectrics, and Frequency Control* 70.10 (2023), pp. 1229–1238. DOI: `10.1109/TUFFC.2023.3245809` (cit. on p. 20).

[27] W. P. Su, J. R. Schrieffer, and A. J. Heeger. «Solitons in Polyacetylene». In: *Phys. Rev. Lett.* 42 (25 June 1979), pp. 1698–1701. DOI: `10.1103/PhysRevLett.42.1698`. URL: `https://link.aps.org/doi/10.1103/PhysRevLett.42.1698` (cit. on p. 23).

[28] Christopher Hakoda, Joseph Rose, Parisa Shokouhi, and Clifford Lissenden. «Using Floquet periodicity to easily calculate dispersion curves and wave structures of homogeneous waveguides». In: *AIP Conference Proceedings* 1949.1 (Apr. 2018), p. 020016. ISSN: 0094-243X. DOI: `10.1063/1.5031513`. eprint: `https://pubs.aip.org/aip/acp/article-pdf/doi/10.1063/1.5031513/13849049/020016\_1\_online.pdf`. URL: `https://doi.org/10.1063/1.5031513` (cit. on p. 24).

[29] Hongbo Zhang, Bilong Liu, Xilong Zhang, Qianqian Wu, and Xingang Wang. «Zone folding induced tunable topological interface states in one-dimensional phononic crystal plates». In: *Physics Letters A* 383.23 (2019), pp. 2797–2801. ISSN: 0375-9601. DOI: `https://doi.org/10.1016/j.physleta.2019.05.045`. URL: `https://www.sciencedirect.com/science/article/pii/S0375960119304967` (cit. on p. 25).

[30] M. Z. Hasan and C. L. Kane. «Colloquium: Topological insulators». In: *Rev. Mod. Phys.* 82 (4 Nov. 2010), pp. 3045–3067. DOI: `10.1103/RevModPhys.82.3045`. URL: `https://link.aps.org/doi/10.1103/RevModPhys.82.3045` (cit. on p. 32).

[31] Berry M.V. «Quantal phase factors accompanying adiabatic changes». In: *Proc. R. Soc. Lond.* 392 (Nov. 1984), pp. 45–57. URL: `http://doi.org/10.1098/rspa.1984.0023` (cit. on p. 32).

[32] J. Zak. «Berry's phase for energy bands in solids». In: *Phys. Rev. Lett.* 62 (23 June 1989), pp. 2747–2750. DOI: `10.1103/PhysRevLett.62.2747`. URL: `https://link.aps.org/doi/10.1103/PhysRevLett.62.2747` (cit. on pp. 32, 33).

[33] Meng Xiao, Guancong Ma, Zhiyu Yang, Ping Sheng, Z. Q. Zhang, and C. T. Chan. «Geometric phase and band inversion in periodic acoustic systems». In: *Nature Physics* 11.3 (Mar. 2015), pp. 240–244. DOI: `10.1038/nphys3228` (cit. on pp. 33, 34).

[34] Jianfei Yin, Massimo Ruzzene, Jihong Wen, Dianlong Yu, Li Cai, and Linfeng Yue. «Band transition and topological interface modes in 1D elastic phononic crystals». In: *Scientific Reports* 8.1 (May 2018). ISSN: 2045-2322. DOI: `10.1038/s41598-018-24952-5`. URL: `http://dx.doi.org/10.1038/s41598-018-24952-5` (cit. on pp. 33, 34, 36).

[35] R. D. King-Smith and David Vanderbilt. «Theory of polarization of crystalline solids». In: *Phys. Rev. B* 47 (3 Jan. 1993), pp. 1651–1654. DOI: `10.1103/PhysRevB.47.1651`. URL: `https://link.aps.org/doi/10.1103/PhysRevB.47.1651` (cit. on p. 33).

[36] Muhammad, Weijian Zhou, and C.W. Lim. «Topological edge modeling and localization of protected interface modes in 1D phononic crystals for longitudinal and bending elastic waves». In: *International Journal of Mechanical Sciences* 159 (2019), pp. 359–372. ISSN: 0020-7403. DOI: `https://doi.org/10.1016/j.ijmecsci.2019.05.020`. URL: `https://www.sciencedirect.com/science/article/pii/S0020740319306617` (cit. on p. 36).

[37] Muhammad and C. W. Lim. «Analytical modeling and computational analysis on topological properties of 1-D phononic crystals in elastic media». In: *Journal of Mechanics of Materials and Structures* 15.1 (Jan. 2020), pp. 15–35. ISSN: 1559-3959. DOI: `10.2140/jomms.2020.15.15`. URL: `http://dx.doi.org/10.2140/jomms.2020.15.15` (cit. on p. 36).